

Bicameral Structuring and Synthetic Imagery for Jointly Predicting Instance Boundaries and Nearby Occlusions from a Single Image

Matthieu Grard · Emmanuel Dellandréa · Liming Chen

Received: date / Accepted: date

Abstract Oriented boundary detection is a challenging task aimed at both delineating category-agnostic object instances and inferring their spatial layout from a single RGB image. State-of-the-art deep convolutional networks for this task rely on two independent streams that predict boundaries and occlusions respectively, although both require similar local and global cues, and occlusions cause boundaries. We therefore propose a fully convolutional bicameral structuring, composed of two cascaded decoders sharing one deep encoder, linked altogether by skip connections to combine local and global features, for jointly predicting instance boundaries and their unoccluded side. Furthermore, state-of-the-art datasets contain real images with few instances and occlusions mostly due to objects occluding the background, thereby missing meaningful occlusions between instances. For evaluating the missing scenario of dense piles of objects as well, we introduce synthetic data (Mikado), which extensibly contains more instances and inter-instance occlusions per image than the PASCAL Instance Occlusion Dataset (PIOD), the COCO Amodal dataset (COCOA), and the Densely Segmented Supermarket Amodal dataset (D2SA). We show that the proposed

M. Grard
Sileane, 17 rue Descartes F-42000 Saint Étienne, France
Université de Lyon, CNRS, École Centrale de Lyon LIRIS
UMR5205, F-69134 Lyon, France
Tel.: +33 (0)4 77 79 03 71
Fax: +33 (0)4 77 74 50 86
E-mail: m.grard@sileane.com

E. Dellandréa
Université de Lyon, CNRS, École Centrale de Lyon LIRIS
UMR5205, F-69134 Lyon, France

L. Chen
Université de Lyon, CNRS, École Centrale de Lyon LIRIS
UMR5205, F-69134 Lyon, France

network design outperforms the two-stream baseline and alternative architectures for oriented boundary detection on both PIOD and Mikado, and the amodal segmentation approach on COCOA as well. Our experiments on D2SA also show that Mikado is plausible in the sense that it enables the learning of performance-enhancing representations transferable to real data, while drastically reducing the need of hand-made annotations for finetuning.

Keywords Instance boundary and occlusion detection · Fully convolutional encoder-decoder networks · Synthetic training data · Domain adaptation

1 Introduction

Delineating object instances and inferring their spatial layout from a single RGB image is a core computer vision task with a plethora of real-time applications in robotics, autonomous driving, medicine, and more. Automating such a task remains challenging as a robot must handle a broad variability of instance poses, light conditions, textures, and shapes from a mere grid of RGB values. Deep fully convolutional neural networks (FCN) have become the state of the art for instance segmentation in images due to their strong ability to learn non-linear mappings between low-level inputs and object-wise annotations. Two FCN-based paradigms have emerged, considering instance localization as a late or early task respectively, *i.e.* following or preceding instance segmentation. The late-localization paradigm consists in training a FCN to classify each pixel independently of the instance it belongs to, either in binary form by predicting whether it is an instance boundary [1–6], or in a multi-class formulation by assigning a predefined

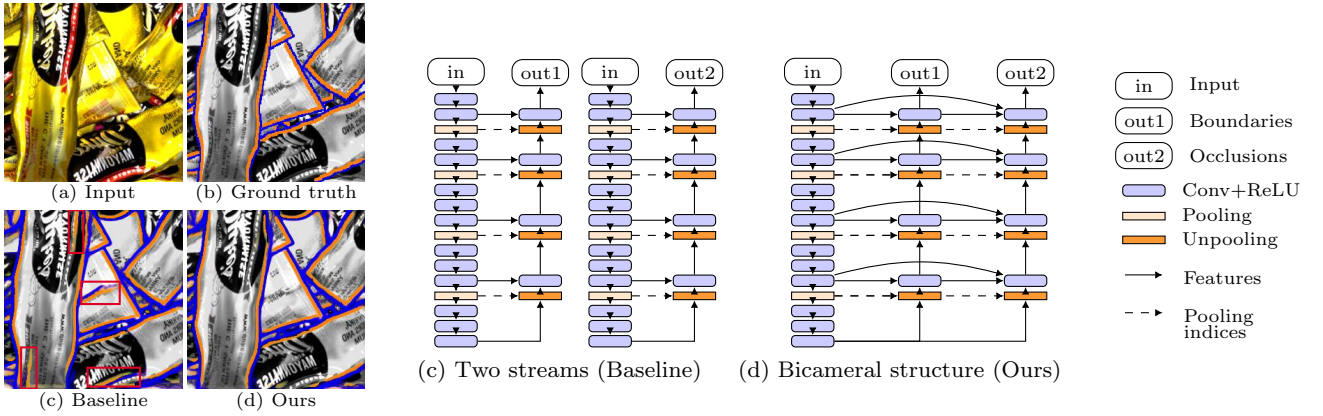


Fig. 1: Example (left) of instance boundary (blue) and unoccluded side (orange) detection using different network architectures (best viewed in color). False positive (in red rectangles) predicted by the two-stream baseline (c) are removed by using instead two cascaded decoders sharing the same encoder (d) as proposed

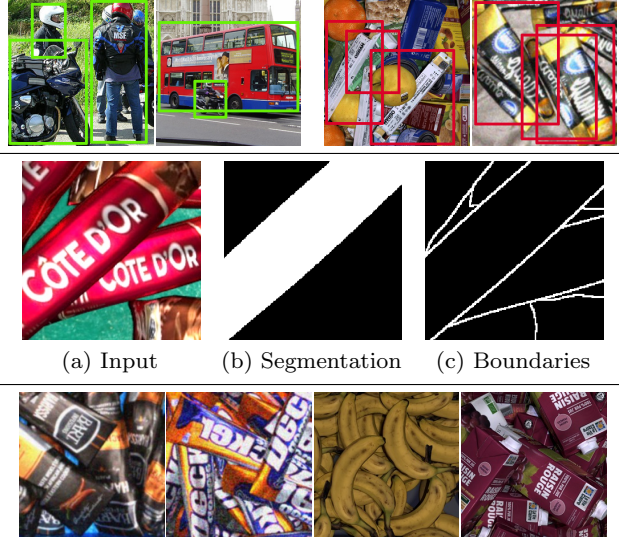
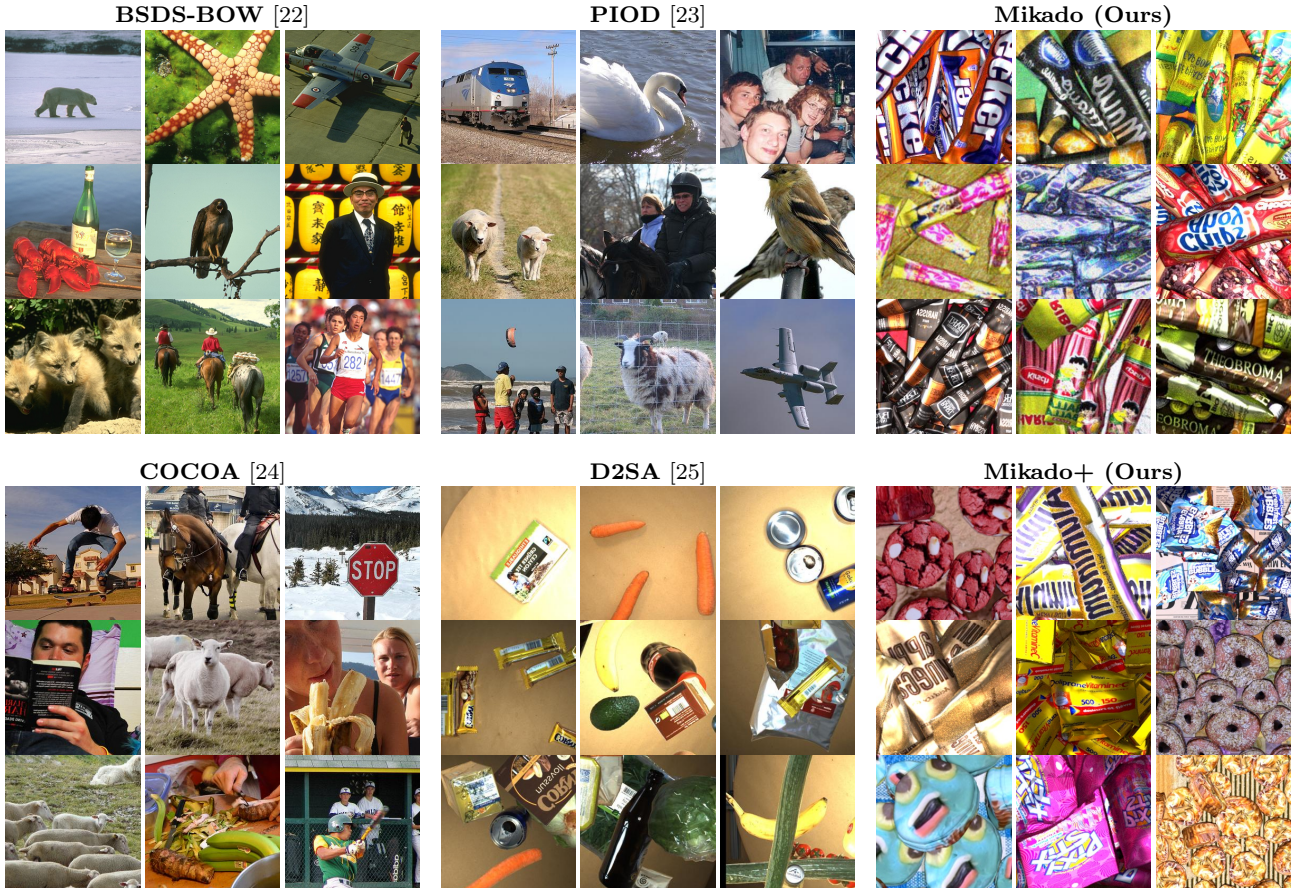


Fig. 2: First row: unlike natural scenes (left) in which most objects fit a rectangle, bounding boxes in piles of objects (right) may often be equally shared by several instances. Second row: state-of-the-art paradigms for delineating instances using a fully convolutional network. Instance boundary detection (c) is better suited for tackling piles of similar objects, as end-to-end segmentation (b) may result in classifying differently similar patterns (a). Third row: other examples of dense piles of objects occluding each other. An instance can occlude other instances and be occluded at the same time

object category [7–10]. Instance segments are then built upon the object boundary or category map, by combinatorial grouping of superpixels [11, 12], learning watershed segmentation [13], or using conditional random fields [14, 15]. Alternatively, instance segmentation has been approached by first isolating each instance [16–20].

This early-localization approach typically consists in using a “region proposal” sub-network [21] for detecting all the rectangle regions that might contain an object, and then a second sub-network for ranking and binarizing each region proposal such that each pixel is classified as being part of the instance or not, relatively to the predicted bounding box. However, coloring all the pixels of an instance becomes an ambiguous task if several instances occluding each other equally share the same region proposal, as illustrated in Figure 2. Unlike people or cars in natural scenes, an instance in a pile does not often fit a rectangle as it can remain at rest in any pose. Furthermore, when a manufactured object is instantiated multiple times like often in robotic setups, it may mean as a consequence classifying differently similar patterns, inconsistently with the translation invariance property of convolutional layers. An instance in a dense pile of objects occluding each other may also occlude other instances and be partially occluded at the same time. Consequently, in order to finely understand the spatial relations with each neighboring instance, occlusions must be defined at boundaries. For all these reasons, we consider in this work a FCN for classifying pixels as instance boundary or not, but also for inferring their nearby spatial layouts as a local binary problem.

Augmenting instance boundaries with an orientation indeed enables the network to not only separate object instances but also embed a local depth perception by learning to order the boundary sides on a virtual depth axis, from a single RGB image. Similarly to two-stream network architectures aimed at fusing different modalities [26, 27], state-of-the-art networks for this task rely on two independent streams that predict boundaries and occlusions separately. Concretely, in the late-localization paradigm, it consists in detecting respectively the in-



| Dataset | Average image size | Number of images | Number of instances | Instances per image | Inter-instance occlusions per image | Background pixels per image | Ground-truth annotations |
|-----------------------------------|--------------------|------------------|---------------------|---------------------|-------------------------------------|-----------------------------|--------------------------|
| BSDS-BOW ¹ [22] | 432×369 | 200 | — | — | — | — | Human-made |
| PIOD [23] | 469×386 | 10,100 | 24,797 | 2.5 | 1.3 | 69% | |
| COCOA ² [24] | 578×483 | 3,823 | 34,884 | 9.1 | 13.5 | 33% | Computer-generated |
| D2SA ² [25] | 1962×1569 | 5,600 | 28,703 | 5.1 | 2.8 | 79% | |
| Mikado (Ours) | 640×512 | 2,400 | 48,184 | 20.1 | 52.9 | 24% | Computer-generated |
| Mikado+³ (Ours) | 640×512 | 14,560 | 459,002 | 31.5 | 60.5 | 24% | |

¹ the empty cells are due to the ground truth that consists only in object part-level oriented edges² the statistics are only on the train and validation subsets as the test subset is not provided³ Mikado+ is an extension of Mikado used only to show the impact of a richer synthetic data distribution

Fig. 3: Samples and characteristics of state-of-the-art datasets for oriented boundary detection [22, 23] and amodal instance segmentation [24, 25] compared to our synthetic dataset. Unlike the state-of-the-art datasets in which occlusions are mostly due to objects occluding the background, Mikado contains more instances and occlusions between instances per image, thus better representing the variety of occlusions

stance boundaries and their orientation [23]. In the early-localization paradigm, it consists in coloring respectively the visible instance mask and the mask including both the visible and invisible instance parts [28], namely the modal and amodal masks. However, occlusions are a major source of instance boundaries. Considering occlusions jointly with boundaries could thus provide much

richer information for scene understanding, as in a few works prior to the use of FCN [29, 30]. Humans indeed leverage shadows and partially occluded patterns to instantly detect object boundaries and guess simultaneously the spatial relations between instances. Moreover, in state-of-the-art solutions, an instance-wise orientation is assigned to object boundaries in natural scenes for

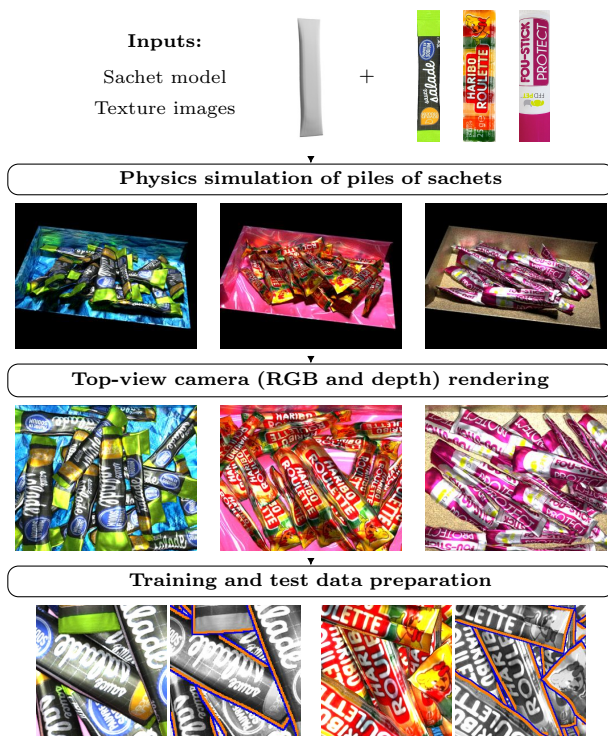


Fig. 4: Overview of the Mikado pipeline (best viewed in color). Given a mesh template and texture images, piles of deformed instances are generated using a physics engine. A top-view camera is then rendered to capture RGB and depth. The synthetic images and their annotations (ground-truth boundaries are in blue, unoccluded side in orange) are finally prepared to be fed-forward through the network

mostly describing which side is foreground, and which side is background [23, 31]. In contrast with previous works, we aim at addressing scenes composed of many instances occluding each other, like in robotic setups, in which the background is often hidden. In such configurations, the network should learn to answer instead the more general question “which side is above/before and which one is below/behind?”. We therefore explore in this paper novel FCN architectures for learning instance boundaries and occlusions in a joint feature space, and expectedly reaching better performances on both natural scenes and piles of many instances. Merging boundaries and occlusions in one training would also result in reducing the number of parameters, hence faster training at equal hardware and less redundancies during backpropagation. Nevertheless, inferring fine-grained oriented boundaries from a single RGB image using only a FCN is challenging, because encoding object-level semantics with a FCN requires pooling layers for feature aggregation that gradually compress the spatial information.

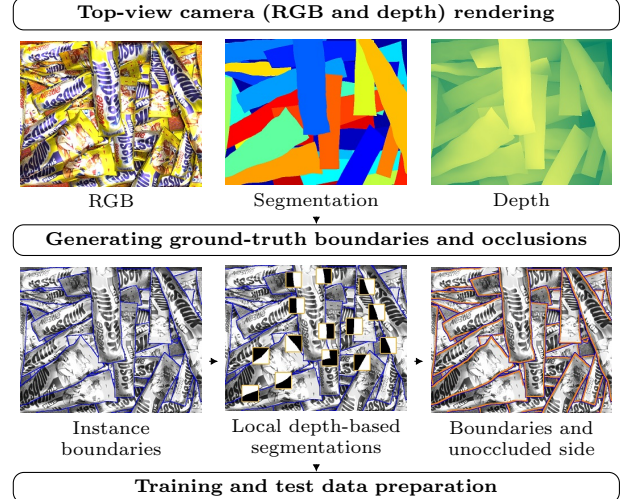


Fig. 5: Pipeline for generating the ground-truth boundaries and occlusions (best viewed in color). At each boundary pixel, a depth-based binary segmentation of the neighborhood is performed to label each side, such that the higher side is set to 1 and the lower side to 0. In the end, the ground truth consists of instance boundaries (blue) and their unoccluded side (orange)

State-of-the-art networks for unoriented instance boundary detection [1, 2] are therefore derived from encoder-decoder structuring [4, 8], whose decoder is aimed at gradually recovering accurate object-level boundaries by inversely leveraging the encoder feature maps. [2, 5] notably introduced residual-like connections [32] between the encoder and the decoder, advocating the superiority of such connections over sequential structuring [4, 8] and holistically-nested connections [3, 6] (*c.f.* Figure 6). Starting from [23], which proposed two independent encoder-decoder streams with holistically-nested connections, we build our two-stream baseline by replacing their holistically-nested connections by residual-like ones, consistently with the state of the art on single-stream networks. We then propose a novel *bicameral* structuring for jointly inferring boundaries and occlusions, consisting in one encoder shared by two cascaded decoders through multiple skip connections, as illustrated by Figure 1.

Furthermore, state-of-the-art datasets for oriented boundary detection [23, 31], and amodal segmentation [24, 25], are intrinsically designed for the foreground/background paradigm insofar as the number of instances per image is limited and a large number of occlusions are due to objects occluding the background, as shown by Figure 3. However, various applications in robotics often address the case of dense piles of many instances, in which the background is much less visible and oc-

clusions are mostly between instances. Moreover, these datasets suffer from biased data distributions due to a limited content and error-prone hand-made annotations. They can also hardly be extended, as producing a pixel-wise ground truth for both instance boundaries and occlusions is a tedious and time-consuming task for human annotators. In order to better study occlusions between instances, that are insufficiently represented in the aforementioned datasets, we highlight the scenario of many instances piled up in bulk by introducing an effective simulation-based pipeline, referred to as Mikado. We show not only that the proposed network design outperforms our baseline on both the state-of-the-art real-world datasets and Mikado, but also that Mikado is plausible in the sense of an effective transferability to real data by a simple domain adaptation. In summary, our contribution in this work is three-fold:

- a performance-enhancing *bicameral* network design, consisting in two cascaded decoders sharing one deep encoder, linked altogether by skip connections, for jointly predicting instance boundaries and their unoccluded side;
- synthetic data, referred to as Mikado, with extensibly more inter-instance occlusions per image than the PASCAL Instance Occlusion Dataset (PIOD) [23] and the COCO Amodal dataset (COCOA) [24], for better studying occlusions between instances;
- extensive experiments: on both PIOD and Mikado for comparing network designs, including the state-of-the-art approach [23] and a number of alternative designs; on COCOA for comparing with the state-of-the-art proposal-based approach [24] referred to as amodal segmentation; on the D2S Amodal dataset (D2SA) [25] for showing that Mikado is plausible for real-world applications.

Our paper is organized as follows. After reviewing the state of the art in Section 2, we describe the proposed dataset in Section 3, the proposed network design in Section 4, and our experimental protocol in Section 5. Results are then discussed in Section 6.

2 Related Work

In this section, we review the state-of-the-art approaches for detecting occlusions from single images, designing and training a FCN for inferring full-resolution pixel labels, and making annotated data for oriented boundary detection.

Occlusion detection Finding occlusion relations has mostly been studied jointly with depth estimation in multi-view contexts [34–36] and motion sequences [37–43], as

occlusions often translate into missing pixel correspondences in different points of view or consecutive frames. Some recent works have more ambitiously focused on predicting a dense depth map from a monocular image [44–46], but the results are still less accurate than standard multi-view 3D reconstruction algorithms, and these techniques require ground-truth depth maps difficult to obtain. Considering a single point of view for inferring occlusions instead of accurate distances from the camera seems however more prone to success, as occlusions consist in binarized differences of depth at object boundaries while still conveying the notion of depth ordering. [22] firstly proposed a two-stage approach consisting in using an edge detector [47] to extract gradient-based features for a conditional random field (CRF) that performs local foreground/background classifications. Because local gradient-based features are limited for understanding occlusions, [48] introduced 3D cues within a similar procedure, by making assumptions on the global 3D structure of the scene (sky, ground). Observing that detecting objects and foreground/background occlusions are actually coupled tasks, object part segmentation and figure/ground organization were later recovered in a single step using angular embedding [30]. However, as angular embedding and CRFs both require expensive computational time at large scales, [29] suggested a faster simultaneous edge and foreground/background detection by leveraging structured random forests [49], but still using hand-crafted features derived from a limited set of contour token clusters. More recently, in order to avoid human biases when defining features, a convolutional neural network (CNN) was instead employed to produce contextual feature representations [31] or to learn pixel-centric pairwise relations for affinity and figure/ground embedding [50]. Towards end-to-end training, and in the footsteps of fully convolutional networks (FCN) for pixel-wise classification, two approaches have lately emerged. The first approach [24], namely amodal instance segmentation, follows the two-step early-localization paradigm of region proposal-based instance segmentation, but aims instead at predicting for each instance the mask including both the visible and the non-visible instance parts. An estimation of the instance occlusion rate can then be obtained by comparing the predicted modal (visible parts only) and amodal masks. This approach however cumulates the drawbacks of region-based instance segmentation, discussed in our introduction, and the difficulty of coloring something invisible, thus resulting in low instance boundary accuracy. The second approach [23] follows the late-localization paradigm and consists in a two-stream FCN that predicts independently boundaries and their occlusion-based orientation in one forward pass. More precisely, [23] set up one

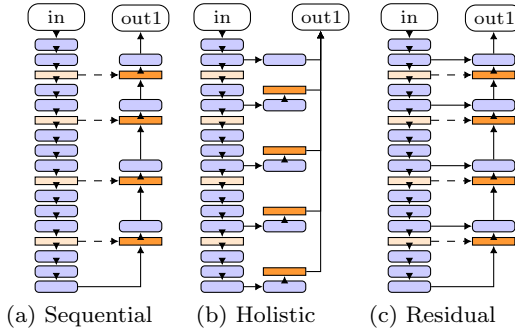


Fig. 6: State-of-the-art encoder-decoder architectures for instance boundary detection (best viewed in color), using a VGG16-based [33] encoder. Legend is the same as Figure 1

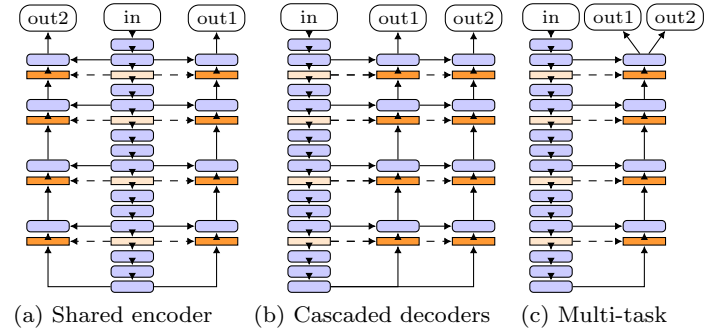


Fig. 7: Alternative architectures also considered for jointly predicting boundaries and occlusions (best viewed in color), using a VGG16-based [33] encoder and a residual-like structure as decoder template. Legend is the same as Figure 1

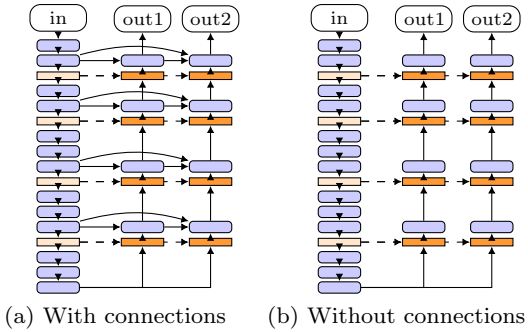


Fig. 8: A bicameral structure with (a) and without (b) residual-like connections between the encoder and decoders (best viewed in color). Legend is the same as Figure 1

stream of the network to predict the raw orientation of a local unit vector specifying the occlusion relations by a left-hand rule, and used a logistic loss function that strongly penalizes wrong directions but only weakly tangent directions. However, to ensure a local continuity, the orientation predictions have to be further “adjusted” using the local tangent vectors of the predicted boundaries as the network may not predict similar orientations for neighbourhood pixels. There is indeed no constraints ensuring a local continuity of the network prediction, all the more as the ground-truth orientation map is noisy itself. To overcome this issue and remove any post-processing step, we propose instead to reformulate the occlusion prediction as a local binary segmentation problem near boundaries. Both modelled as binary maps, boundaries and occlusions can then be detected using a single fully convolutional encoder-decoder structure equipped with residual-like connections, *i.e.* the proposed bicameral design, thus efficiently sharing features instead of using two independent encoders.

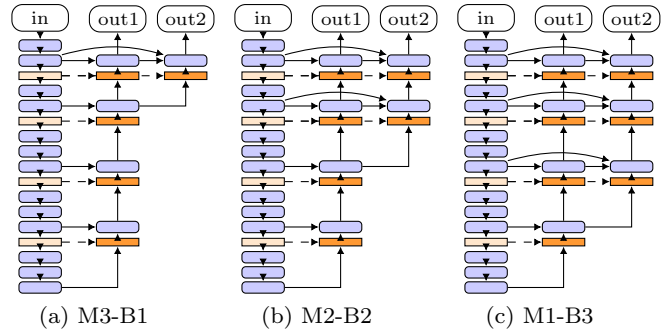


Fig. 9: Hybrid architectures that merge multi-task (“M”) and bicameral (“B”) decoder designs at different stages, using a VGG16-based [33] encoder (best viewed in color). Legend is the same as Figure 1

Encoder-decoder networks Inspired by auto-encoders for unsupervised representation learning, encoder-decoder networks have been firstly introduced for single-task setups, such as semantic segmentation [8] and instance contour detection [4], in order to recover accurate boundaries despite the resolution loss when encoding object-level semantics. The encoder produces deep hierarchical features, and the decoder gradually outputs a binary or category map using symmetric unpooling stages (*c.f.* Figure 6a). To keep the upsampling efficient, the decoder typically uses max-unpooling layers that take the pooling indices from the encoder max-pooling layers. However, such an architecture requires the network to restore accurate boundaries only from the last encoder activation maps, where information is the most spatially compressed. Instead of a progressive decoding, [3, 6] introduced holistically-nested connections for a late fusion of all the encoder feature maps upsampled to the image scale, thus giving a multiscale view to the decoder (Figure 6b). Similarly to two-stream designs aimed at fusing



Fig. 10: Sachet texture (top) and background (bottom) images used for generating the proposed Mikado dataset

different modalities [26, 27], the two-stream baseline for oriented boundary detection [23] employed independent encoder-decoder streams with holistically-nested connections. This architecture however hardly allows for learning a joint feature representation of boundaries and occlusions due to direct connections between each intermediate feature map and the output layer from which starts the backpropagation. In the context of semantic segmentation, [51] proposed to merge local and global semantics through a dual-task training, consisting in jointly decoding pixel labels and inferring image labels after the encoder. Image-level classification is however unfeasible in our object category-agnostic problem, although detecting instance boundaries and inter-instance occlusions require global cues as well. Combining progressive upsampling with connections to the latent feature representations at each scale can be achieved al-

ternatively by residual-like connections [32] between the encoder and decoder (Figure 6c), as proposed in single-task networks [1, 2, 5]. Residual-like connections notably proved to be superior to holistically-nested ones for single-stream encoder-decoder networks [2]. Indeed, by giving each decoder stage access to both the upsampled previous one and the corresponding encoder activation maps, the network can gradually merge the higher-level semantics of the previous scale with the spatial information lost during encoding at the current scale. Performing such a combination besides reduces the checkerboard artifacts inherent to unpooling [52]. In contrast with two independent multiscale streams, the proposed bicameral design employs skip connections to combine local and higher-level cues from a single feature space for detecting both boundaries and nearby occlusions.

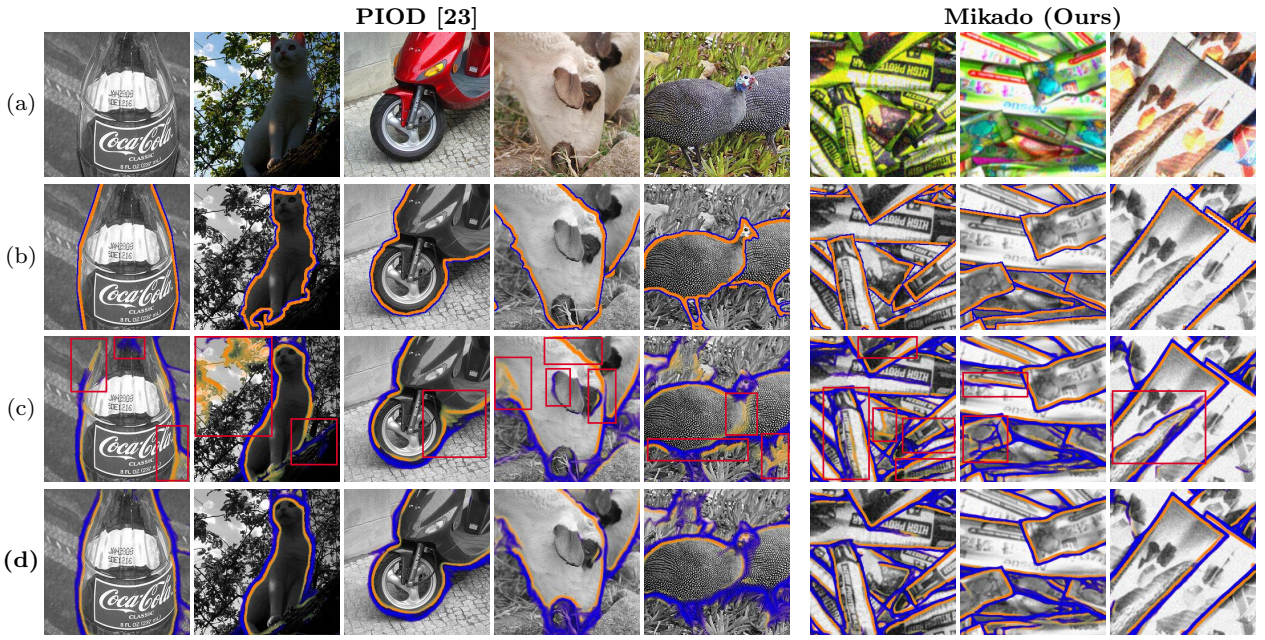


Fig. 11: Comparative results for instance boundary (blue) and unoccluded side (orange) detection on PIOD and Mikado (best viewed in color). From top to bottom: input (a), ground truth (b), prediction using the two-stream baseline (c), using the proposed architecture (d). Red rectangles highlight some false positive predicted by the baseline network that are erased when cascading decoders

| Architecture | Number of parameters | PIOD [23] | | | Mikado (Ours) | | |
|--------------------------|-----------------------------|----------------|---------------|----------------|---------------|----------------|---------------|
| | | Boundaries ODS | Boundaries AP | Occlusions ODS | Occlusions AP | Boundaries ODS | Boundaries AP |
| Two streams (Baseline) | 46,839,938 ($\times 1.0$) | .673 | .708 | .681 | .733 | .755 | .832 |
| Shared encoder | 32,125,250 ($\times .69$) | .692 | .732 | .686 | .738 | .769 | .847 |
| Cascaded decoders | 29,949,250 ($\times .64$) | .694 | .735 | .689 | .748 | .766 | .844 |
| Multi-task decoder | 23,420,770 ($\times .50$) | .691 | .731 | .679 | .731 | .767 | .845 |
| Bicameral decoder | 34,301,250 ($\times .73$) | .697 | .738 | .692 | .747 | .769 | .847 |
| | | | | | | .801 | .884 |

Table 1: Best F-score on dataset scale (ODS) and average precision (AP) for instance boundary and occlusion detection on two datasets using different architectures. The bicameral decoder, which combines a shared encoder and cascaded decoders, outperforms the two-stream baseline and a multi-task decoder as well

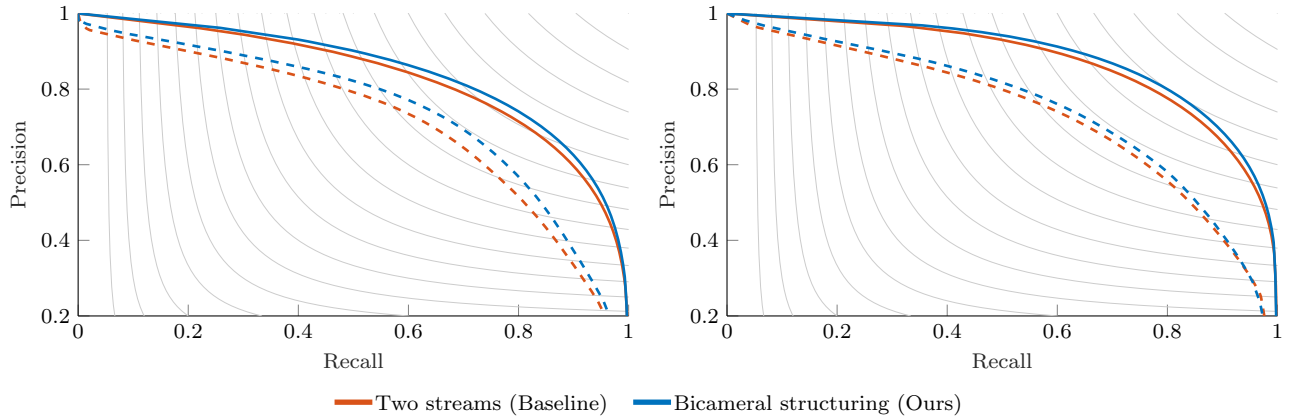


Fig. 12: Precision-recall curves for instance boundary (left) and unoccluded side (right) detection on PIOD (dashed lines) and Mikado (solid lines) using different architectures (best viewed in color)

| Architecture | Encoder backbone | Number of parameters | Boundaries | | | Occlusions | | |
|------------------------|------------------|-----------------------------|-------------|-------------|------------------|-------------|-------------|------------------|
| | | | ODS | AP | AP ₆₀ | ODS | AP | AP ₆₀ |
| Two streams (Baseline) | VGG16 [33] | 46,839,938 ($\times 1.0$) | .673 | .708 | .476 | .681 | .733 | .518 |
| | | 34,301,250 ($\times .73$) | .697 | .738 | .517 | .692 | .747 | .532 |
| Bicameral decoder | DenseNet121 [53] | 33,009,846 ($\times .70$) | .712 | .761 | .529 | .714 | .778 | .556 |

Table 2: Best F-score on dataset scale (ODS) and average precision (AP) for instance boundary and occlusion detection on PIOD [23] using different backbones. Plugging a bicameral decoder to a deeper encoder with dense blocks [53] enables to capture a finer representation of the object boundaries and nearby occlusions

| Architecture | Number of parameters | PIOD [23] | | | | Mikado (Ours) | | | |
|------------------------|-----------------------------|-------------|-------------|-------------|-------------|---------------|-------------|-------------|-------------|
| | | Boundaries | | Occlusions | | Boundaries | | Occlusions | |
| | | ODS | AP | ODS | AP | ODS | AP | ODS | AP |
| Two streams (Baseline) | 46,839,938 ($\times 1.0$) | .673 | .708 | .681 | .733 | .755 | .832 | .788 | .872 |
| Multi-task decoder | 23,420,770 ($\times .50$) | .691 | .731 | .679 | .731 | .767 | .845 | .795 | .880 |
| M3-B1 hybrid decoder | 23,548,802 ($\times .50$) | .691 | .735 | .683 | .734 | .767 | .845 | .796 | .879 |
| M2-B2 hybrid decoder | 24,060,866 ($\times .51$) | .692 | .738 | .685 | .740 | .769 | .848 | .797 | .881 |
| M1-B3 hybrid decoder | 26,108,994 ($\times .56$) | .693 | .737 | .685 | .739 | .771 | .848 | .802 | .885 |
| Bicameral decoder | 34,301,250 ($\times .73$) | .697 | .738 | .692 | .747 | .769 | .847 | .801 | .884 |

Table 3: Best F-score on dataset scale (ODS) and average precision (AP) for instance boundary and occlusion detection on two datasets using different levels of layer sharing between the branches of a bicameral decoder

Loss functions Beyond the scope of this work but worth mentioning, recent works [1, 54] focused on novel loss functions for learning crisper and thinner boundaries without post-inference step. Due to the imbalanced distribution of boundary and non-boundary pixels, training FCNs for object boundary detection is commonly driven by a balanced cross-entropy loss function, but it produces thick edges, ultimately thinned by non-maximum suppression [2–6, 23]. To address this concern, [1, 54] respectively introduced the Dice loss, which basically compares the similarity between two sets, and edge alignment during training by solving a minimum cost bipartite assignment problem. In the context of object detection, which faces the same class-imbalance issue, [55] also introduced the so-called focal loss to put more focus on the hard misclassified training examples. In this work, we focus on the network architecture and training data, and leave for future work the introduction of these novel loss functions. In all our experiments, we use balanced cross-entropy loss functions, but perform evaluation without non-maximum suppression, which may artificially improve precision, as presented in Section 4.

Datasets Occlusion boundary detection from a single image raised interest with the BSDS Border Ownership dataset (BSDS-BOW) [22], derived from the BSDS500 dataset [56] for object contour detection, which contains 200 natural images manually annotated with object part-level oriented contours. As state-of-the-art FCNs require more training data, [23] recently presented a dataset larger than BSDS-BOW, namely the PASCAL Instance Occlusion Dataset (PIOD), comprising about 10,000 manually annotated natural images from the

PASCAL VOC Segmentation dataset [57]. Similarly for amodal instance segmentation, [24, 25] have proposed real-world datasets, namely the Densely Segmented Supermarket Amodal dataset (D2SA) and the COCOA Amodal dataset (COCOA). These latter datasets are subsets of much larger datasets for instance segmentation in the early-localization paradigm, COCO [58] and D2S [25] respectively, but augmented with the ground-truth amodal annotations, that can be derived for oriented boundary detection (*c.f.* Section 5). Despite their challenging instance intra-class variability, the support images contain few instances and are limited in terms of inter-instance occlusions. However, in robotic setups, scenes are often composed of many instances occluding each other. Applying on such scenes a model trained on PIOD or COCOA would give poor results since these datasets provide mostly foreground/background boundary examples for training. As extending hand-labeled real-world datasets is a time-consuming task, D2SA partly alleviates this concern by artificially overlaying manually delineated instances for creating fake images with more instances, but at the cost of lighting inconsistencies at instance boundaries. The images from these datasets suffer besides from missing or ambiguous ground-truth annotations, thereby introducing a human bias during training and test. To address these issues, synthetic datasets [59, 60] have emerged for learning and evaluation as they offer a fully controlled environment and a perfect ground truth. Recently proposed for evaluating pose detection and estimation, the Siléane dataset [60], generated using Blender [61], consists of top-view depth maps depicting piles of many rigid in-

stances of some CAD models. Similarly, [59] compared methods for end-to-end instance segmentation from synthetic depth maps of scanned objects instantiated in bulk. From these observations, we propose to make and use synthetic data for oriented boundary detection from a single image, emphasizing inter-instance occlusions that are under-represented in the state-of-the-art datasets.

3 The Mikado Data

In this section, we describe the proposed pipeline for generating the synthetic Mikado data, and its extension Mikado+.

Data generation Similarly to [59, 60], we generate synthetic data using custom code on top of Blender [61] by simulating scenes of objects piled up in bulk and rendering the corresponding top views, as depicted in Figure 4. More precisely, after modelling a static open box and, on top, a perspective camera, between 2 and 40 object instances, in random initial pose, are successively dropped above the box using Blender’s physics engine (a video showing the generation of a scene is provided in supplementary material). We then render the camera view, and the corresponding depth image, using Cycles render engine. In this configuration, we ensure a large pose variability, a lot of inter-instance occlusions, and the ground-truth occlusion boundaries can be trivially derived from depth.

However, differently from [59, 60], we consider here piles of many instances with inner variability and using only RGB. We generate RGB images of sachets piled up in bulk by randomly applying global and local deformations to one mesh template of sachet that we texture successively with one out of 120 texture images of sachets retrieved using the Google Images search engine¹ and manually cropped to remove any background. Each scene is composed of many instances using the same texture image so as to make the occlusions between instances more challenging to detect. Besides, to prevent the network from simply subtracting the background, we apply to the box a texture randomly chosen among 40 background images, retrieved using the Google Images search engine as well. A comprehensive overview of the textures and background images used for generating the dataset is provided in Figure 10. Between each image generation, we also randomly jitter the cameras and light locations to prevent the network from learning a fixed source of light, and so fixed reflections and shadows. The proposed dataset finally comprises on average

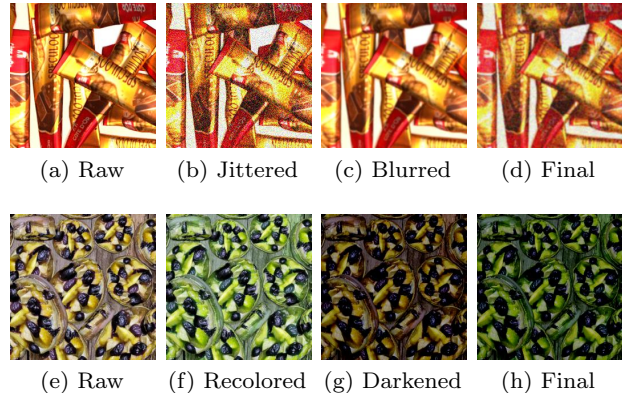


Fig. 13: First row: to avoid overfitting the noise-free generated pixels, value jittering (b) and gaussian blur (c), using random parameters within predefined intervals, are successively applied (d) on our synthetic images (a). Second row: in Mikado+ only, random under/overexposure (f) and RGB channel permutation (g) are both applied as well (h) to enrich the generated data distribution (e).

| | Mikado | Mikado+ |
|----------------|--------|---------|
| Mesh templates | 1 | 4 |
| Backgrounds | 40 | 600 |
| Textures | 120 | 2,400 |
| Images | 2,400 | 14,560 |

Table 4: Differences between the proposed Mikado data and its extension Mikado+

20.1 instances per image, hence 8 times more instances and 40 times more inter-instance occlusions per image than PIOD. Figure 3 provides samples and sums up the Mikado characteristics compared to the state-of-the-art datasets for oriented boundary detection [23, 31] and amodal instance segmentation [24, 25].

Furthermore, to study the benefits of a richer synthetic data distribution, we additionally make an extension of Mikado, namely Mikado+ (*c.f.* Figure 3), following the same proposed generation pipeline but using more mesh templates (sachet, square sachet, box, cylinder-like shape), and more texture and background images. Table 4 sums up the differences between Mikado and Mikado+.

Data augmentation As our RGB images are generated using heuristic rendering models, the training and evaluation may be biased by a lack of realism in the sense that, unlike physical sensors and despite the large variability of textures, deformations, and simulated specular reflections, a noise-free pixel information is provided to

¹ <https://images.google.com/>

the network. To remedy this issue, we dynamically filter one image out of two with a gaussian blur and jitter independently the RGB values, as shown in Figure 13, randomly at both training and testing time. The parameters for gaussian filtering and value jittering are randomly chosen within empirically predefined intervals. This prevents the network from overfitting the too perfect synthetic color variations. In addition to dynamic blurring and RGB jittering, the Mikado+ images are also augmented with random permutation of the RGB channels and random under or over-exposition, as also illustrated by Figure 13. Unlike Mikado, Mikado+ thus depicts more color and lighting variations as well.

Data plausibility check We create Mikado for evaluating the scenario of many similar instances piled in bulk. Such a scenario, often encountered in real-world robotic applications such as bin-picking, is missing from PIOD and COCOA. In a limited manner, D2SA addresses this case by overlaying manually isolated instances into fake training images [25]. To compare with this augmentation strategy, that we refer to as D2SA+, and show that the proposed synthetic data is plausible for real-world applications, we evaluate the transferability of features learned from Mikado to real data. In line with [62], features learned from a source domain are transferable if they can be repurposed and boost generalization on a target domain. Specifically, we train the proposed network on Mikado, then retrain on D2SA only the decoders and some of the top encoder blocks, as deep features transition from general to specific by the last layers. Furthermore, as a proof of the benefits of synthetic data in contrast with hardly extensible real-world datasets, we study how a richer synthetic data distribution, *i.e.* Mikado+, impacts the domain adaptation. As the ranges of texture, shape, and pose variations are more widely represented in Mikado+, better transferable invariants are expected to be learned.

4 Network Design

In this section, we first describe the proposed bicameral structuring in contrast with the two-stream baseline and alternative network designs. Second, we detail our loss function compared to the baseline.

Bicameral structuring and alternative designs Along strong texture variations and shadows, partially hidden patterns are also cues for understanding both boundaries and occlusions between object instances but they require a more global perception to be detected. Meanwhile, detecting an occlusion can be interpreted as assigning a relative depth to the sides of a flat separation between

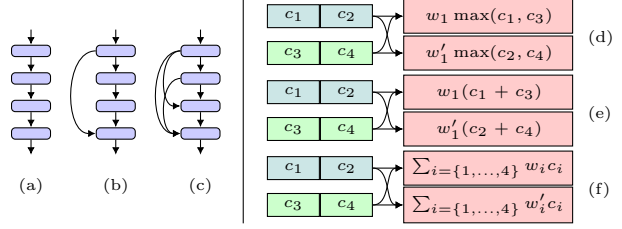


Fig. 14: Left: state-of-the-art convolutional block types: sequential [33] (a); residual [32] (b); dense [53] (c). Right: skip connection types, here for linearly merging, using parameters w_i and w'_i , two 2-channel feature vectors (c_1, c_2) and (c_3, c_4) into a new 2-channel one (red): by element-wise max (d); by element-wise sum (e); concatenation (f). Best viewed in color

two instances. We therefore argue that separating instances and detecting occlusions are intrinsically chained tasks, that could rely upon a common scene representation. From these core intuitions, we introduce a novel network design, referred to as *bicameral* structuring, that jointly infers instance boundaries and the local depth ordering of their sides, as depicted in Figure 1d. More precisely, a bicameral structuring is composed of two cascaded decoders, chained together and to one deep encoder with skip-layer connections between each unpooling stage. As occlusions are often near boundaries, the first decoder is assigned to boundaries, and the second decoder in cascade to predict their unoccluded side. In order to assess the roles of feature sharing and cascaded decoding in the proposed network design, we compare the proposed bicameral architecture with four alternative architectures:

- a two-stream encoder-decoder (Fig. 1c), *i.e.* our baseline introduced in [23], for which the streams are dedicated to boundaries and occlusions respectively;
- a network with two independent decoders sharing the same encoder (Fig. 7a);
- two decoders in cascade after one encoder (Fig. 7b);
- a multi-task decoder that predicts both boundaries and occlusions (Fig. 7c).

Encoder backbone For fair comparison, each network has the same VGG16-based [33] encoder, and is equipped with residual-like [32] connections, also referred to as skip connections, between the encoder and the decoder(s) for progressively combining local and global features when decoding. Note that we arbitrarily choose VGG16 as backbone for our experiments, but any backbone is virtually suitable. To advocate this claim, we compare bicameral designs with a VGG16-based and DenseNet121-based encoder respectively. In contrast with VGG16,

which interleaves sequential convolutional blocks and pooling layers, DenseNet121 [53] emphasizes the concept of residual connections by introducing multiple residual connections inside each convolutional block, resulting in a deeper chain of dense blocks. The differences between sequential, residual and dense convolutional blocks are illustrated in Figure 14. Following our network representation in Fig. 1, we point out that, if we describe skip connections in a dense block as “vertical” dense connections, then bicameral connections, *i.e.* skip connections between the decoders and the encoder, can then be interpreted as “horizontal” dense connections.

Decoder(s) All the compared networks share the same convolutional hyperparameters for their decoder(s). Specifically, for each decoder, the kernel of each convolutional layer is a 5×5 square, and the four convolutional blocks have, respectively from bottom to top, 256, 128, 64 and 32 filters. We additionally assess whether feature sharing can apply to the branches of a bicameral decoder by comparing hybrid architectures that merge multi-task and fully bicameral designs (Figure 9).

Skip connections To study what skip connections bring in the bicameral structuring, we compare bicameral designs with and without such connections (Figure 8). We also try out different skip connection types (*c.f.* Fig. 14): concatenation (our default choice for all the other experiments); element-wise max; element-wise sum. We choose concatenation by default because one can formally expect element-wise max and sum operations to be obtained using concatenation. Indeed, let $N \in \mathbb{N}^*$ be the depth of two layers to merge, and $e, d, f \in \mathbb{R}^N$ feature vectors respectively for the encoder, the decoder, and the resulting fusion. Let $w, w' \in \mathbb{R}^{N \times N}$ be trainable parameters. Using element-wise max operators, $\forall k \in \{1, \dots, N\}$, $f_k = \sum_{i=1}^N w_{ik} \max(e_{ik}, d_{ik})$. Using element-wise sum operators, $\forall k \in \{1, \dots, N\}$, $f_k = \sum_{i=1}^N w_{ik} (e_{ik} + d_{ik})$. Using concatenation, $\forall k \in \{1, \dots, N\}$, $f_k = \sum_{i=1}^N (w_{ik} e_{ik} + w'_{ik} d_{ik})$. If needed, an element-wise sum operator can then be modelled by setting $w = w'$. Similarly, an element-wise max operator can be obtained by setting $w_{ik} = 0$ or $w'_{ik} = 0$ depending on which of the i th encoder or decoder channel has greater importance.

Loss function As commonly adopted, we use a balanced sigmoid cross-entropy loss function for learning object boundaries as a binary map [2–6]. The two terms of the loss function are weighted in order to counterbalance the low number of boundary pixels against non-boundary pixels. In our experiments, we set these weights such that the “contour pixel” penalty is 10 times more important than the “non-contour” term, regardless of the dataset.

We are aware of more recent loss functions [1, 54, 55] but we leave the introduction of these loss functions for future work.

In the two-stream baseline [23], the stream for occlusions consists in inferring the raw orientation $\theta \in (-\pi, \pi]$ of a local unit vector specifying the occlusion relation by a left-hand rule, independently of the stream for boundaries. Their orientation learning is driven by a logistic loss function that strongly penalizes wrong directions but only weakly tangent directions. However, a consistency check between boundaries and orientations is required after each forward pass, by using the local tangent vectors of the predicted boundaries for adjusting the predicted orientations, since by construction, there is no mechanism enforcing a local continuity of the network prediction.

By using instead a single encoder-decoder structure, and reformulating the occlusion prediction as a local binary segmentation problem close to instance boundary detection, we can overcome this limitation. In practice, near each boundary pixel, we propose to set the side which is above the other one to “1”, and the side below to “0”. More precisely, for generating the ground-truth occlusion binary maps, we sweep all the ground-truth instance boundaries, and for each boundary pixel, we binarize the centered local region by computing the mean Z-offset in each segment of the region. In the end, a ground-truth occlusion map is a binary map whose positive pixels are the instance boundaries slightly translated to one side or another, according to the relative depth difference of the boundary sides, as illustrated by the final ground-truth image in Figure 5. Note that boundary pixels are set to 0 in the occlusion map. Occlusion can then also be learned using a balanced sigmoid cross-entropy loss function.

Formally, let $\mathbf{p} \in \mathcal{P}$ be a pixel location – typically $\mathcal{P} = \{1, \dots, W\} \times \{1, \dots, H\}$ for an image of width $W \in \mathbb{N}^*$ and height $H \in \mathbb{N}^*$ – and $\sigma : \mathbb{R} \rightarrow [0, 1], x \mapsto (1 + \exp(x))^{-1}$ the canonical sigmoid function. We note $\mathcal{N} = \{1, \dots, N\}$ where $N \in \mathbb{N}^*$ is the number of training images, and $M_{\mathbf{p}} \in \mathcal{V}$ the value at location $\mathbf{p} \in \mathcal{P}$ in a matrix $M \in \mathcal{V}^{\mathcal{P}}$. With the proposed formulation for occlusions, the network jointly minimizes two cross-entropy loss functions \mathcal{L}_b (Eq. 1) and \mathcal{L}_o (Eq. 2), respectively for instance boundaries and occlusions, defined as follows:

$$\begin{aligned} \mathcal{L}_b(\theta) = -\frac{1}{|\mathcal{N}||\mathcal{P}|} \sum_{n \in \mathcal{N}} \sum_{\mathbf{p} \in \mathcal{P}} & \alpha Y_{\mathbf{p}}^n \log(\sigma(F_b(X^n, \theta_{\mathbf{p}}))) \\ & + (1 - Y_{\mathbf{p}}^n) \log(1 - \sigma(F_b(X^n, \theta_{\mathbf{p}}))) \end{aligned} \quad (1)$$

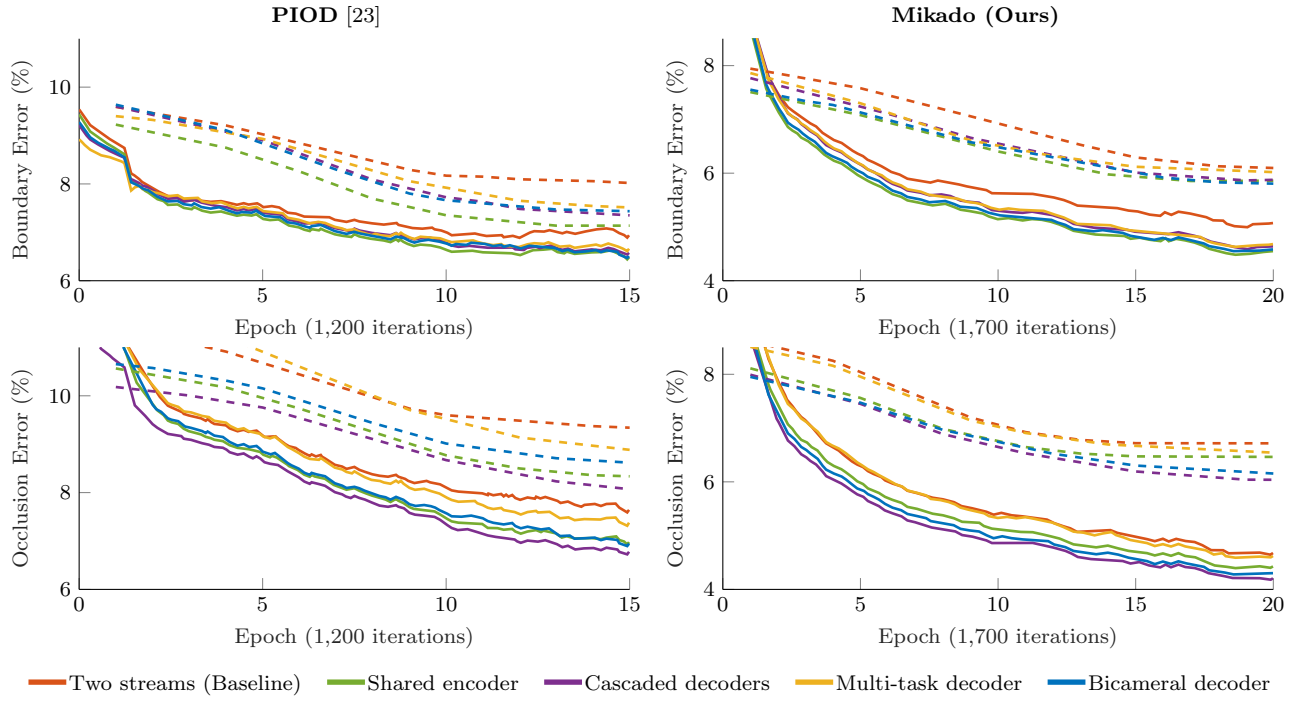


Fig. 15: Training (solid lines) and test (dashed lines) errors for instance boundary (top) and occlusion (bottom) detection on PIOD (left) and the Mikado dataset (right) using different network architectures (best viewed in color). Lower boundary and occlusion errors are reached when jointly predicting boundaries and occlusions (green, blue, yellow, purple) rather than independently (red)

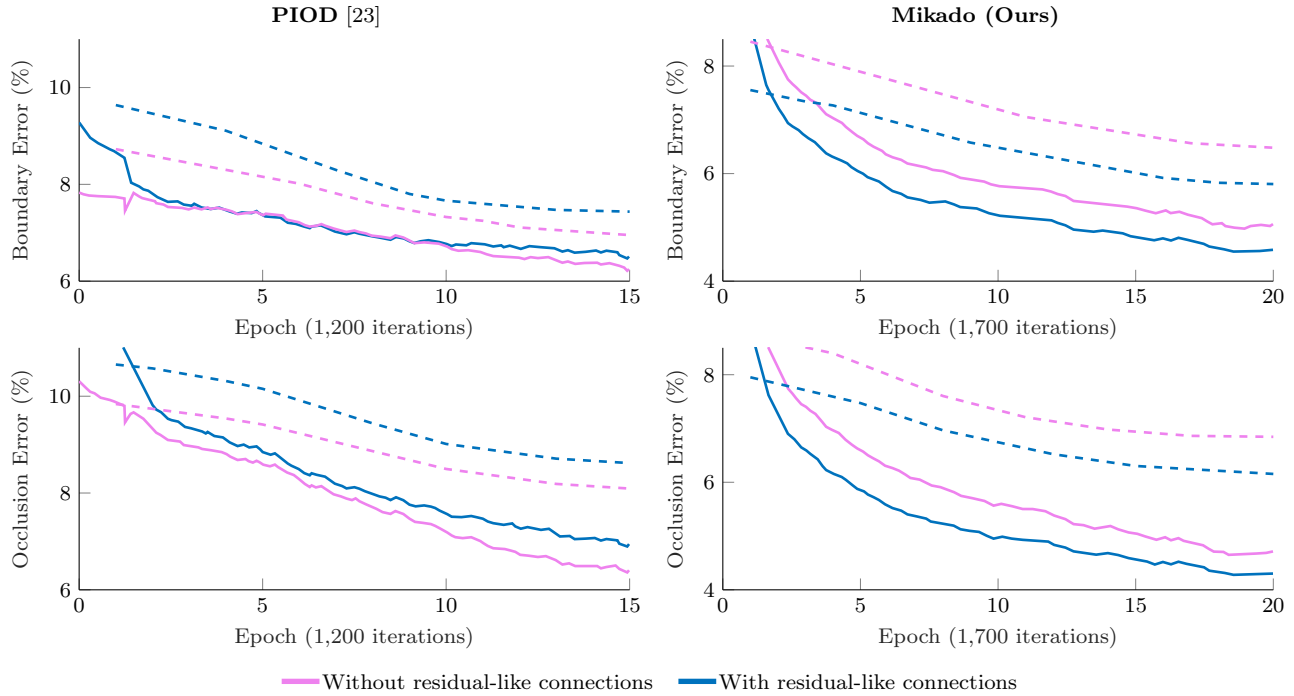


Fig. 16: Training (solid lines) and test (dashed lines) errors for instance boundary (top) and occlusion (bottom) detection on PIOD (left) and the Mikado dataset (right) using a bicameral decoder with and without residual-like connections (best viewed in color). Relatively to the initialization, a better error minimization is achieved when using connections between the encoder(s) and decoder(s) at each scale for learning jointly boundaries and occlusions

$$\mathcal{L}_o(\theta) = -\frac{1}{|\mathcal{N}||\mathcal{P}|} \sum_{n \in \mathcal{N}} \sum_{\mathbf{p} \in \mathcal{P}} \alpha Z_{\mathbf{p}}^n \log(\sigma(F_o(X^n, \theta_{\mathbf{p}}))) + ((\alpha - 1)Y_{\mathbf{p}}^n + 1)(1 - Z_{\mathbf{p}}^n) \log(1 - \sigma(F_o(X^n, \theta_{\mathbf{p}}))) \quad (2)$$

where $\{(X^n, Y^n, Z^n) \in (\mathbb{R}^3)^{\mathcal{P}} \times \{0, 1\}^{\mathcal{P}} \times \{0, 1\}^{\mathcal{P}}\}_{n \in \mathcal{N}}$ is the training dataset of RGB images X^n , associated with their ground-truth binary maps Y^n and Z^n respectively for boundaries and occlusions. If a pixel $\mathbf{p} \in \mathcal{P}$ of the image X^n is an instance boundary then $Y_{\mathbf{p}}^n = 1$, else $Y_{\mathbf{p}}^n = 0$. If \mathbf{p} is the unoccluded side of an instance boundary then $Z_{\mathbf{p}}^n = 1$, else $Z_{\mathbf{p}}^n = 0$. $F_b(X, \theta) \in \mathbb{R}^{\mathcal{P}}$ designates the network prediction for boundaries, and $F_o(X, \theta) \in \mathbb{R}^{\mathcal{P}}$ for occlusions, using the parameters θ . In practice, $\alpha = 10$. The factor $((\alpha - 1)Y_{\mathbf{p}}^n + 1)$ in Eq. 2 ensures consistency with Eq. 1, as we want the intersection between the boundary and occlusion binary maps to be empty. Basically, this factor enables to give the “is-not-unoccluded-side” penalty as much importance as the “is-unoccluded-side” term when a pixel in the occlusion map is a boundary, *i.e.* $Y_{\mathbf{p}}^n = 1$ and $Z_{\mathbf{p}}^n = 0$.

Note that when generating the ground-truth occlusion map, local patches that contain more than two segments are fully set to 0 as they cannot be binarized. This proves to be a reasonable limitation as in practice an overwhelming majority of boundary pixels are between only two instances or between an instance and the background (*e.g.*, 97.1% of the boundary pixels in Mikado, and 99.4% in PIOD). We leave for future work the study of the minority of pixels at the junction of more than two instances.

5 Experimental Setup

In this section, we describe our experiments to evaluate the proposed network architecture and the jointly proposed synthetic data. We design our experimental setup to answer the three following questions:

1. Is the proposed bicameral structuring the best architecture for oriented boundary detection?
2. How does the late-localization paradigm compare with the early-localization paradigm?
3. Is the proposed synthetic Mikado data plausible for real-world applications?

We answer these questions by conducting three sets of experiments for respectively comparing:

1. the proposed bicameral design with our two-stream baseline and alternative architectures, presented in Section 4, on PIOD [23] and Mikado;

2. the proposed bicameral design with the amodal segmentation approach on COCOA [24];
3. different pretraining and finetuning conditions for transfer learning [62] from the proposed synthetic data to real images on D2SA [25].

More precisely, each set of experiments is respectively composed of comparisons between:

1. (a) the bicameral design and our two-stream baseline built from [23] (Fig. 1, 11, 12, 15 and Tab. 1);
 (b) the bicameral design and alternative architectures (Fig. 15 and Tab. 1);
 (c) bicameral designs with different levels of layer sharing in the bicameral decoder (Tab. 3);
 (d) bicameral designs with and without skip connections (Fig. 16, 17, 18 and Tab. 5);
 (e) bicameral designs with different type of skip connections (Fig. 14 and Tab. 5);
 (f) bicameral designs with different encoder backbones (Tab. 2);
2. (a) the bicameral design and the two-stream encoder-decoder network for amodal instance segmentation [24] (Fig. 19, 20 and Tab. 7);
 (b) the bicameral design and the amodal segmentation approach per instance type, *i.e.* things and stuff (Figure 20 and Tab. 7);
3. (a) bicameral networks finetuned on D2SA without and after pretraining on Mikado, with different encoder block at which the network is chopped and retrained (Fig. 22), to expose the most transferable features learned from Mikado (Fig. 21 and Tab. 9);
 (b) bicameral networks finetuned on D2SA using the most transferable synthetic features and different number of finetuning images, to reduce the need of hand-made annotations and compare with the augmentation strategy of [25], referred to as D2SA+ (Fig. 23);
 (c) bicameral networks finetuned on D2SA using the most transferable features learned from Mikado or Mikado+, to show the impact of a richer synthetic data distribution (Mikado+) on domain adaptation (Fig. 23).

Let us finally address some concerns that the reader may have regarding our experimental setup:

- We leave out the BSDS Border Ownership dataset [22] as it contains only 200 images, and mostly because the ground truth does not define instance boundaries but object part-level edges.
- We compare the late and early-localization paradigms only on COCOA because amodal segmentation requires the amodal instance masks, which are not

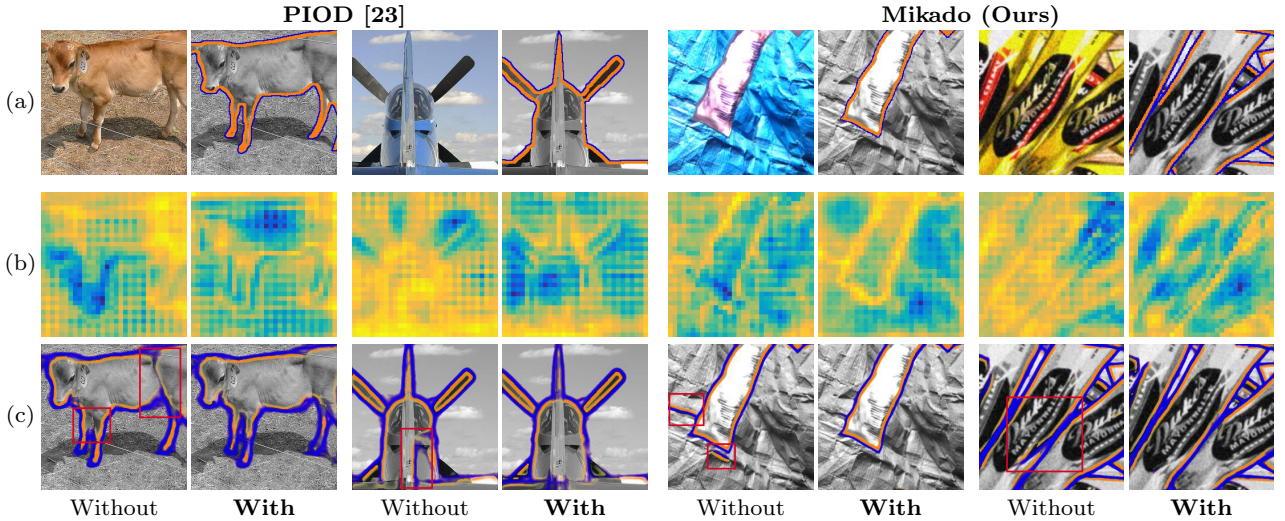


Fig. 17: Comparative results for instance boundary (blue) and unoccluded side (orange) detection on PIOD and Mikado using a bicameral decoder with and without residual-like connections by concatenation (c.f. Figures 6a and 6c). From top to bottom: (a) input and ground truth, (b) activation map after the affine transformation following the first unpooling layer of the boundary branch, (c) final detection. Combining spatial information and higher-level semantics at each scale using residual-like connections between the encoder and decoders enables to detect instance boundaries earlier when decoding

| Residual-like connections? (Type) | PIOD [23] | | | | | | Mikado (Ours) | | | | | |
|-----------------------------------|-------------|-------------|------------------|-------------|-------------|------------------|---------------|-------------|------------------|------------|-------------|------------------|
| | Boundaries | | | Occlusions | | | Boundaries | | | Occlusions | | |
| | ODS | AP | AP ₆₀ | ODS | AP | AP ₆₀ | ODS | AP | AP ₆₀ | ODS | AP | AP ₆₀ |
| No | .693 | .744 | .495 | .692 | .749 | .520 | .759 | .834 | .686 | .793 | .878 | .748 |
| Yes (Element-wise max) | .685 | .729 | .512 | .676 | .731 | .522 | .755 | .830 | .676 | .786 | .871 | .735 |
| Yes (Element-wise sum) | .687 | .730 | .505 | .678 | .731 | .514 | .761 | .838 | .685 | .791 | .876 | .743 |
| Yes (Concatenation) | .697 | .738 | .517 | .692 | .747 | .532 | .769 | .847 | .698 | .801 | .884 | .758 |

Table 5: Best F-score on dataset scale (ODS), average precision (AP) and average precision in high-recall regime (AP₆₀) for instance boundary and occlusion detection on two datasets using a bicameral decoder with and without residual-like connections. Residual-like connections by concatenation between the encoder and the decoder(s) enable to better detect boundaries and occlusions as local and global cues are combined at each scale when decoding

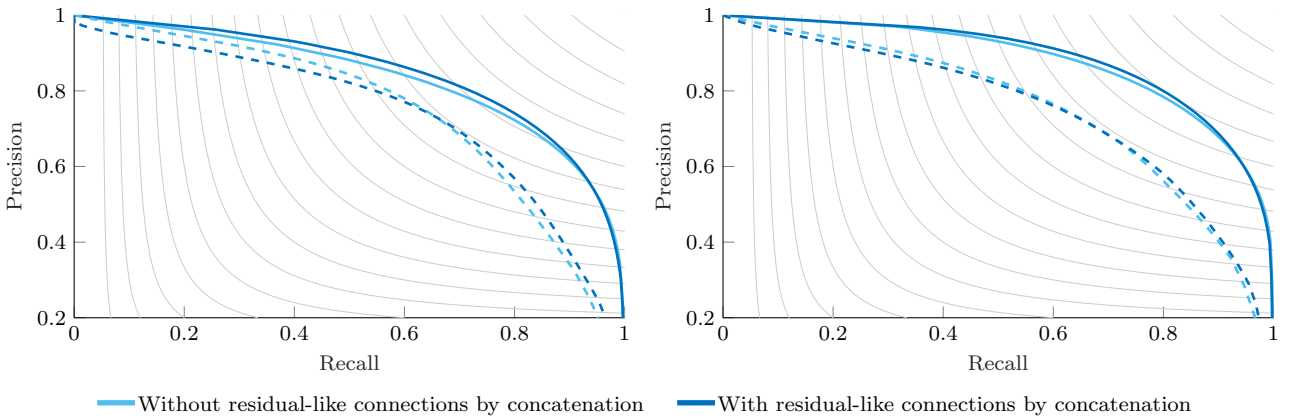


Fig. 18: Precision-recall curves for instance boundary (left) and unoccluded side (right) detection on PIOD (dashed lines) and Mikado (solid lines) using a bicameral decoder with and without residual-like connections by concatenation between the encoder and decoders (best viewed in color)

| |  |  |  |  |  |  |
|-----------------------------|---|---|---|--|---|---|
| | Mikado | PIOD [23] | COCOA [24] | D2SA [25] | D2SA+ ¹ [25] | Mikado+ |
| Training images | 13,600 | 9,600 | 12,800 | 512 | 2,960 | 28,800 |
| Validation images | 800 | 800 | 1,424 | 56 | 328 | 4,800 |
| Test images | 4,800 | 800 | 1,323 | 5,992 | 5,992 | — |
| Training iterations | 34,000 | 18,000 | 24,000 | 960 | 5,550 | 108,000 |
| Training epochs | 20 | 15 | 15 | 15 | 15 | 30 |
| In experiments ² | 1a–f | | 2a–b | | 3a–c | |

¹ refers to the augmentation strategy of [25], consisting in creating fake images by overlaying isolated instances

² refers to the experiments presented in Section 5

Table 6: Per-dataset folds for our cross-validation experiments after offline data augmentation

available in PIOD and not generated in Mikado. For training the proposed network on COCOA and comparing with amodal segmentation, we turn both the COCOA ground truth and the precomputed results of [24] into oriented instance boundaries.

– We consider D2SA instead of PIOD or COCOA for transfer learning from Mikado because the texture, shape, and pose distributions of PIOD and COCOA are very different from Mikado. Indeed, [63, 64] show that a low divergence between the source and target domain distributions is a necessary condition for the success of domain adaptation. Table 8 empirically shows that this condition is not met for Mikado and PIOD. Unlike PIOD and COCOA, which contain natural images of indoor and urban scenes with people, cars and animals, D2SA and Mikado both contain top-view images of household objects in bulk.

Data preparation To robustly assess the generalizability of each model, each experiment is cross-validated using three folds, except for the amodal segmentation results as we use the precomputed binary outputs made publicly available by the authors. To present more significative results when comparing architectures, curves and scores are averaged on the three folds. For training, the networks are not directly fed with the original images but several sub-images randomly extracted from each original image, and augmented offline with random geometric transformations (flipping, scaling and rotation). Note that performances are not impacted by cropping given that the networks are fully convolutional. Table 6 details the folds for each dataset and the related experiments. We also point out some experiment-dependent details:

- Folds of Mikado and Mikado+ are defined such that a texture appears only in one of the three subsets.
- Folds of PIOD, COCOA and D2SA are defined with respect to the initial split proposed by their authors.

Specifically, the original training images are used for training or validation in our folds, and the original validation images for test. The original test images are never used as they are not publicly available.

- For comparing with amodal segmentation, we use the precomputed binary outputs made publicly available by the authors. We derive the oriented boundaries from both the COCOA ground truth and their precomputed results alike: after intersecting the modal and amodal masks of an instance, amodal pixels that don’t belong to the intersection are considered closer to the camera than the pixels of the intersection. This gives an orientation to the instance boundaries, *i.e.* the boundaries of the modal mask.
- When finetuning on D2SA in experiments 3a–c, we define a block as a set of convolutional layers between two pooling layers; a VGG16-based encoder is therefore composed of 5 blocks (*c.f.* Fig. 22). A block is said “frozen” when its corresponding parameters remain unchanged during finetuning.

Training settings For each dataset and each experiment, each network is trained and tested using Caffe [66], and the exact same settings (including fixed random seeds). At training time, we use the Adam solver [67] with $\beta_1 = .9$, $\beta_2 = .999$, $\epsilon = 10^{-8}$, a fixed learning rate of 10^{-4} , a weight decay of 10^{-4} , a ℓ_2 regularization, and a batch size of eight 256×256 images. The training images are randomly permuted at each epoch. As we solve a non-convex optimization problem, without theoretical convergence guarantees, the number of training iterations is chosen for each dataset from an empiric analysis on training and validation subsets. As generally adopted, the optimization is stopped when the validation error stagnates or increases while the training error keeps decreasing. Please note that although the chosen stopping criterion may not be optimal for reaching the best performances on each dataset, it is however sufficient for sig-

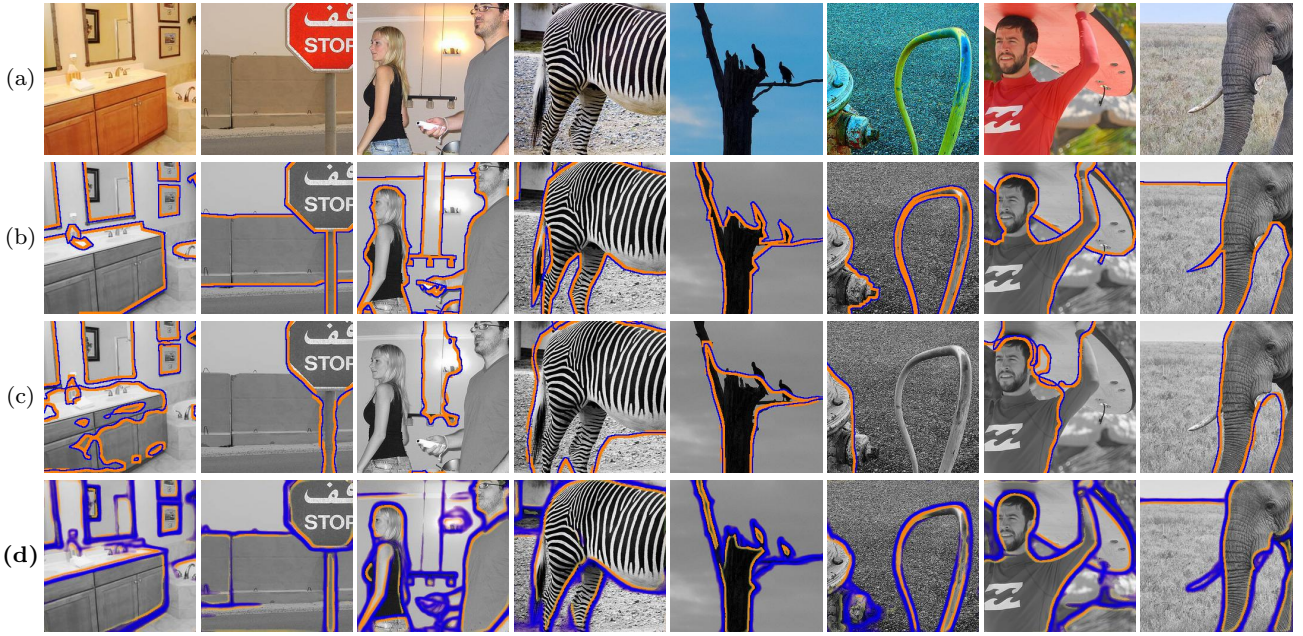


Fig. 19: Comparative results for instance boundary (blue) and unoccluded side (orange) detection on COCOA (best viewed in color). From top to bottom: input (a), ground truth (b), prediction by amodal instance segmentation [24] (c), prediction using the proposed network (d). Unlike the proposed approach, using a region proposal-based detection qualitatively leads to coarse segmentations and non-detected instances

| Approach | All regions | | | | Things ¹ only | | | | Stuff ¹ only | | | |
|---------------------------------------|-------------|------|-------------|------|--------------------------|------|-------------|------|-------------------------|------|-------------|------|
| | Boundaries | | Occlusions | | Boundaries | | Occlusions | | Boundaries | | Occlusions | |
| | ODS | AP | ODS | AP | ODS | AP | ODS | AP | ODS | AP | ODS | AP |
| Amodal segmentation [24] ² | .492 | — | .529 | — | .536 | — | .608 | — | .489 | — | .397 | — |
| Ours | .666 | .694 | .637 | .673 | .666 | .690 | .640 | .674 | .687 | .727 | .648 | .693 |

¹ things are objects with well-defined shape (e.g. car, person) and stuff instances amorphous regions (e.g. grass, sky) [65]

² the evaluation is performed on the binary segment proposals made available by the authors

Table 7: Comparative performances for instance boundary and unoccluded side detection on COCOA [24]. Whereas the proposed network equally performs on things and stuff, oriented boundary detection by amodal instance segmentation tends to focus on things and miss stuff instances

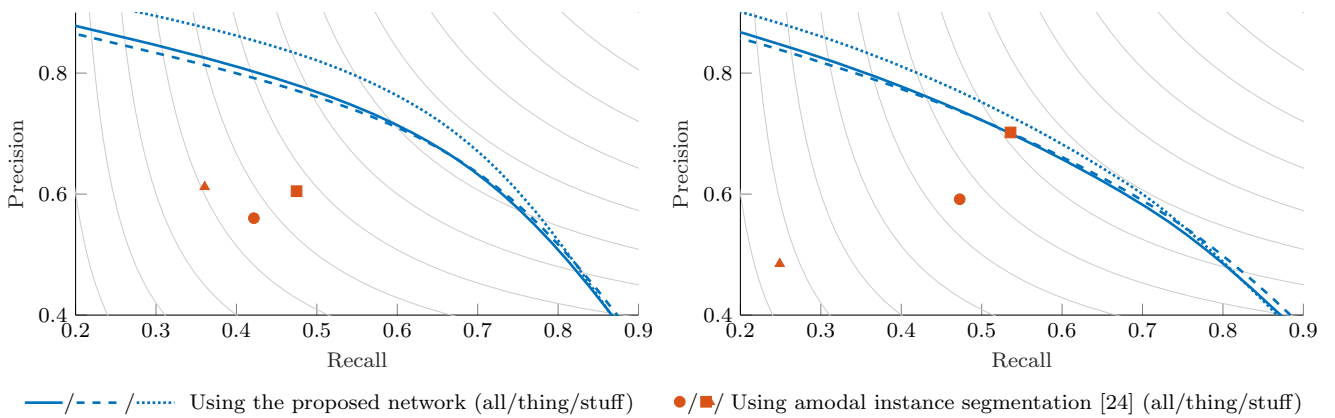


Fig. 20: Precision-recall curves for instance boundary (left) and unoccluded side (right) detection on COCOA comparing bicameral structuring against amodal instance segmentation [24]. Best viewed in color

nificative comparative performances on a given dataset since each network in a comparison is trained under the exact same conditions. For all experiments, except finetuning from weights pretrained on Mikado or Mikado+ in experiments 3a–c, each network has its encoder initialized with weights pretrained on ImageNet [68], and its decoder(s) with the Xavier method [69]. The decoders are also equipped with dropout layers (with a ratio of 0.5) after each convolutional block at training time, to avoid overfitting.

Evaluation metrics As commonly adopted [4, 6, 49, 70–76] since [47], we compute at test time precision and recall, and typical derived metrics: the best F-score on dataset scale (ODS) and the average precision (AP). Whereas ODS highlights one binarization threshold that gives the best compromise between recall and precision, AP conveys the area under the precision-recall curve over the full recall interval. For some experiments, we also consider the average precision in high-recall regime (AP₆₀), that is the precision averaged on the recall interval [0.6, 1]. As matching tolerance, *i.e.* the maximum ℓ_2 -distance to the closest ground-truth pixel for a pixel predicted positive to be considered as a good hit, we consider a hard value of 0 pixels for Mikado (which contains perfect ground-truth boundaries) but a state-of-the-art value of $\tau = 0.0075\sqrt{W^2 + H^2} (\approx 2.7 \text{ pixels in our evaluations})$ for PIOD, COCOA and D2SA that contain approximative hand-made annotations, where $W \in \mathbb{N}^*$ and $H \in \mathbb{N}^*$ are respectively the image width and height. We perform evaluation without non-maximum suppression, which may artificially improve precision.

6 Discussion

In this section, we argue in light of our experimental results that the proposed bicameral structuring is the best design for oriented boundary detection and that the jointly proposed synthetic data is plausible for real-world applications.

Shared encoding features instead of independent streams Our comparative experiments between single encoder-based designs (Fig. 1 and 7) and independent streams (Fig. 1) confirm that separating instances and inferring their spatial layout can be done with a single scene representation. Figure 15 shows that using a shared encoder, multi-task, cascaded or bicameral design instead of the two-stream baseline results in reaching lower boundary and occlusion test errors on both PIOD and Mikado. This is corroborated by Table 1 where the proposed bicameral and alternative architectures outperform the baseline by more than 2 points in ODS and AP, on

both PIOD and Mikado for boundary detection. The joint feature representation can reach a higher expressive power using a deeper encoder composed of dense blocks, instead of sequential ones (Fig. 14). Table 2 reports a gain in AP of more than 6 points for boundaries and more than 4 points for occlusions over the two-stream baseline when building the bicameral encoder on Densenet121 [53] instead of VGG16 [33]. This also illustrates that a bicameral structuring can apply to any encoder backbone, whatever the depth and the type of convolutional blocks.

Bicameral structuring instead of alternative designs

A closer look at Figure 15 shows that the cascaded design reaches the lowest occlusion test error on both PIOD and Mikado. This suggests that chaining occlusion to boundary detection eases the backpropagation for occlusion prediction, as the decoder for occlusions may leverage a hierarchical feature representation of flat instance boundaries instead of undecoded image features. A gain in AP is achieved by cascaded decoders over the baseline (1.5 point up on PIOD, 1 point up on Mikado) but also the shared encoder design (1 point up on PIOD) for which decoders are independent. However, Table 1 shows that cascaded decoders are slightly less efficient for detecting boundaries on Mikado than a multi-task decoder or two independent decoders sharing the same encoder. This is explained by the impossibility of the occlusion decoder to influence directly the encoder blocks. This trade-off is overcome by the bicameral design, which combines cascaded decoders both directly linked to the single encoder and has consequently the largest area under the precision-recall curve in Figure 12. The proposed bicameral structuring also outperforms a multi-task design. Table 1 notably reports that merging decoders limits the expressive power in favor of boundaries on PIOD. The obtained scores are well illustrated by the comparative predictions in Figure 11 where one can observe more closed boundaries and many false positive, mostly occlusions, predicted by the baseline and removed when instead decoding in cascade from a joint feature space.

Partially shared or independent decoding features A bicameral structuring outperforms a multi-task design but one may also wonder whether partial feature sharing can apply to the bicameral decoder branches. Table 3 presents the performances obtained with three hybrid architectural variations between multi-task and bicameral designs (Fig. 9), each one introducing feature sharing at different levels of decoding. On PIOD, a bicameral decoder remains superior to all hybrid decoders, notably by about 1 point higher in ODS and AP for

| | | Tests on Mikado (Ours) | | | | Tests on PIOD [23] | | | | | |
|----------------------|--|-------------------------------|------|------------|------|---------------------------|--|------------|------|------------|------|
| Trained on | | Boundaries | | Occlusions | | Trained on | | Boundaries | | Occlusions | |
| | | ODS | AP | ODS | AP | | | ODS | AP | ODS | AP |
| Mikado (Ours) | | .769 | .847 | .801 | .884 | PIOD [23] | | .697 | .738 | .692 | .747 |
| PIOD [23] | | .300 | .233 | .326 | .267 | Mikado (Ours) | | .405 | .350 | .400 | .349 |

Table 8: Cross-dataset performances between Mikado and PIOD using a bicameral design. Both datasets perform poorly on each other because they follow very different texture, shape, and pose distributions



Fig. 21: Comparative results for instance boundary (blue) and unoccluded side (orange) detection on D2SA (best viewed in color). From top to bottom: input (a), ground truth (b), prediction using the proposed network trained on D2SA (c), using the proposed network pretrained on Mikado then finetuned on D2SA with the first three encoder blocks frozen (d). Pretraining the proposed network on Mikado before finetuning on D2SA leads to a visually significant improvement in the quality of the results

occlusions. On Mikado, sharing the first bottom decoder stage (M1-B3 design), which conveys object-level semantics, slightly improves performances. This suggests that the task specialization, for boundaries and occlusions respectively, may occur at a more local scale in decoding, either because of the higher density of inter-instance occlusions in Mikado, or due to the shape similarity of the Mikado instances. Unlike any of the hybrid designs, the bicameral decoder nevertheless achieves strong ODS and AP on both PIOD and Mikado. We thus advise to consider boundaries and occlusions separately by default after unpooling the encoder feature maps with lowest resolution.

Skip connections for combining local and global cues
 Partially hidden patterns are a major source of boundaries and occlusions. A perception at both local and global scales is however required to understand that

an instance is partially occluded. By construction, an encoder-decoder network combines local and global cues by stacking convolutional and pooling/unpooling layers. This combination is enhanced by residual-like connections at each scale between the encoder and decoder(s), as it enables to gradually combine the unpooled higher-level semantics with the spatial information lost after pooling. Figure 17 qualitatively shows what such connections bring: instance boundaries are detected earlier, thus giving the network more flexibility to adjust the following transformations and activations towards the desired output. These observations are corroborated by the scores in Table 5 and the precision-recall curves in Figure 18. A bicameral structuring with residual-like connections (Figure 8a) outperforms a bicameral design without such connections (Figure 8b) by 1 point in ODS and AP on Mikado. The obtained scores on PIOD are here impacted by the encoder initialization, which was

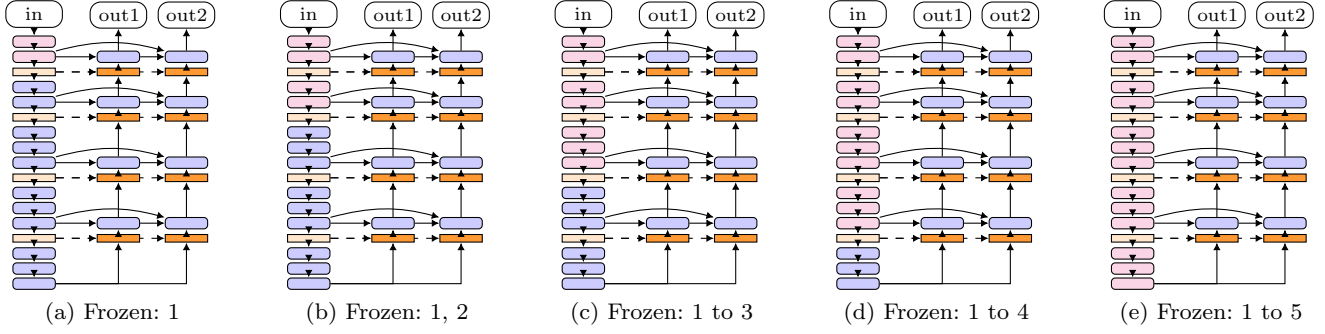


Fig. 22: A bicameral structure with different frozen encoder blocks (best viewed in color). Frozen convolutional layers are in pink. The rest follows the same legend as Figure 1

| Pretraining on Mikado | Finetuning on D2SA [25] | Number of real training images | Frozen encoder blocks* (Fig. 22) | Boundaries | Occlusions |
|-----------------------|-------------------------|--------------------------------|----------------------------------|--------------|--------------|
| | | 438 | None | ODS | AP |
| No | Yes | Augmented (D2SA+) [25] | .700 .783 | .715 .792 | .725 .785 |
| | No | 0 | — | .652 | .649 |
| Yes | Yes | 438 | None | .780 | .808 |
| | | | 1 | .783 | .803 |
| | | | 1, 2 | .780 | .802 |
| | | | 1, 2, 3 | .793 | .819 |
| | | | 1, 2, 3, 4 | .759 | .799 |
| 1, 2, 3, 4, 5 | .767 | .815 | | | |
| | | | | .773 | .823 |

* a block is a set of convolutional layers between two pooling layers; a VGG16-based encoder is therefore composed of 5 blocks

Table 9: Comparative performances of the proposed network on D2SA [25] using different pretraining conditions. Performances on both boundaries and occlusions are maximized when freezing at finetuning time the first three encoder blocks pretrained on Mikado

obtained using a skip-connection free architecture. As a result, the backpropagation flow along the skip connections drastically reshapes the encoder from the first iteration, whereas the encoder of the skip connection-free design is only slightly affected by the backpropagation signals coming from the decoders. This mostly impacts the scores on PIOD because the encoders are initialized with weights pretrained on ImageNet, whose object type and context distributions are much closer to PIOD than Mikado. The skip connection-free design thereby starts to train on PIOD with already meaningful image features, unlike the bicameral design with skip connections on PIOD and both designs on Mikado. Figure 16 indeed reports that the bicameral network without skip connections starts with a lower training error on PIOD. Despite this disadvantage at training time, a bicameral design with residual-like connections shows a better precision in high-recall regime on PIOD, as shown by Figure 18. Table 5 confirms a gain of more than 1 point in AP₆₀ when adding skip connections.

Concatenation instead of alternative merging operators
In all of our experiments, we consider skip connections by concatenation instead of alternative operators (Fig.

14), because we formally expect better performances from concatenation (*c.f.* Section 4). Table 5 confirms our expectation: concatenation produces better experimental results than element-wise sum or max operators. Enforcing sum or max operations indeed introduces arbitrary correspondences between the feature channels to merge. As a result, the low-level encoder activations may be overconsidered in the decoder, thus generating more false positives. Concatenation, as proposed, leaves more degrees of freedom for merging the channels, as each weight for their linear combination before activation is learned during backpropagation. Skip connections that turn out irrelevant can thus be switched off by the decoder, with near-zero weights.

Late instead of early instance localization Another state-of-the-art approach [24] for instance boundary and occlusion detection, referred to as amodal instance segmentation, follows instead an early-localization paradigm. It consists in first detecting rectangle regions that contain an instance, then inferring for each proposal the corresponding modal and amodal masks, *i.e.* respectively the visible instance parts and the mask including both the visible and invisible instance parts. Our comparative

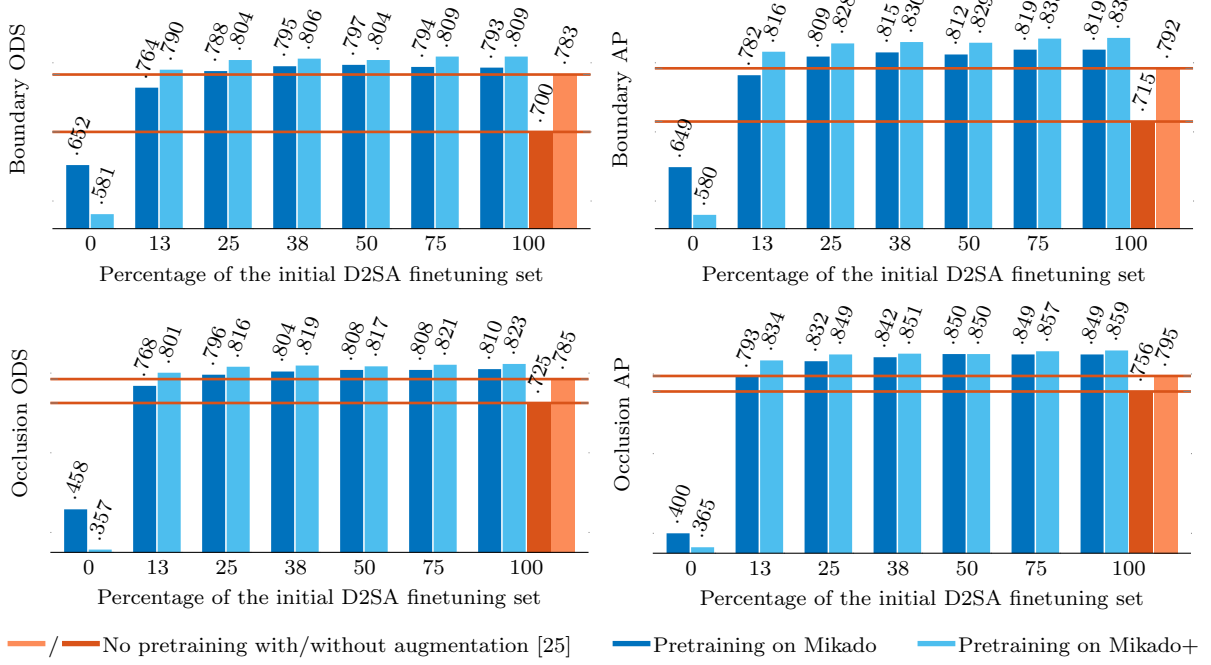


Fig. 23: Performances of the proposed bicameral network pretrained on Mikado/Mikado+ then finetuned on D2SA with the encoder blocks 1, 2, 3 frozen, with respect to the number of real images retained for finetuning. Exploring a wider range of configurations in simulation (Mikado+) enables to learn more abstract local representations of the boundaries and occlusions, thus achieving state-of-the-art performances while drastically reducing the number of real images for finetuning. Best viewed in color

experiments however show that, unlike the proposed approach, amodal segmentation leads to coarse and non-detected boundaries, as illustrated by Figure 19. These observations are corroborated by Table 7 and Figure 20 that report a gain in ODS of 17.4 points for boundaries and 10.8 points for occlusions using our approach. Amodal segmentation indeed conveys the drawbacks of region proposal-based segmentation, in particular: misdetections and non-detections due to errors from the region proposal network; binary segmentations inconsistent with the translation invariance property of convolutional layers if the box proposal contains several instances. This latter ambiguity is compounded when amodally coloring an instance, as a pixel which actually hides an instance should be activated although it belongs to another instance. The proposed network overcomes these limitations by postponing instance localization: each pixel is jointly classified as boundary or not and assigned with an occlusion-based orientation independently of the instance bounding box it belongs to. In addition, amodal segmentation employs a two-stream network whose streams are independent and dedicated to modal and amodal segmentations respectively, similarly to our baseline for oriented boundary detection. When comparing the modal and amodal masks for es-

timating the occlusion rate of an instance, mismatches between the two masks are very likely to occur, thus inducing false positive in the boundary and occlusion maps. Moreover, per-category scores in Table 7 highlight that amodal segmentation leads to better results on things than stuff while the proposed network performs equally on both classes. The stuff category indeed includes amorphous regions (pieces of grass, clouds, walls) that can be missed by the region proposal generator or considered as background when inferring the binary segmentation of a region.

Synthetic data instead of hand-made annotations As Mikado is a computer-generated dataset, one may raise the question whether it is realistic. The answer is obviously no, but we argue that it is plausible for both a significative evaluation and real-world applications. First, when comparing network designs, the same overall relative results are obtained on PIOD, a dataset of manually annotated natural images. Second, the synthetic features learned from Mikado can be repurposed for inference on real images. Specifically, Mikado enables a transferable feature learning in line with [62], *i.e.* first training the network on a source dataset, then retraining only the task-specific layers on the target

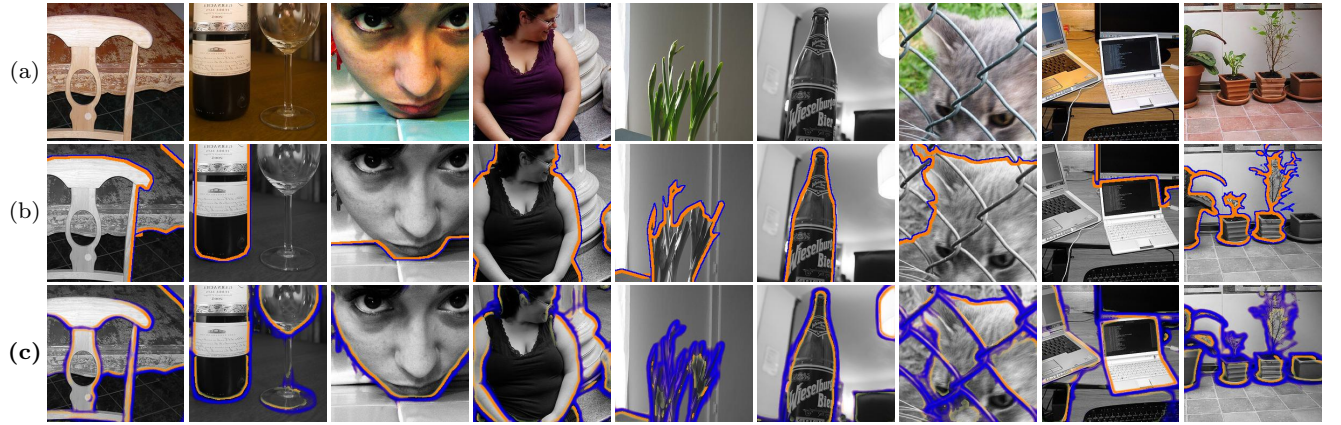


Fig. 24: Instance boundaries (blue) and their unoccluded side (orange) detected using our architecture (c) on PIOD images (a), annotated by humans (b). The proposed network is able to fairly predict non-annotated boundaries and better delineate instances coarsely annotated by humans. Best viewed in color

one. In our transfer learning experiments, we show that using local features pretrained on Mikado enables much better results on D2SA, a dataset of real-world piles of supermarket items [25]. As reported by Table 9 and qualitatively corroborated by Figure 21, a gain of more than 10 points in AP for boundaries and 9 points for occlusions is achieved when finetuning the proposed network on D2SA with the first three encoder blocks frozen (*c.f.* Figure 22) after pretraining on Mikado, instead of training all the layers only on D2SA. This suggests that a network trained on Mikado can learn a more general concept of depth ordering as our dataset presents a wider variety of occlusion relations, including both inter-instance and object/background boundaries. [25] also introduces an augmentation procedure to enrich the training subset with more piles of objects (D2SA+). Their procedure consists in creating new images by overlaying manually isolated instances. Table 9 reports that our simulation-based pretraining outperforms D2SA+ as well. Despite the domain shift, simulation enables more physics-consistent rendering at boundaries and less redundancy in terms of poses, unlike brute-force overlaying of instance segments from real images. Furthermore, almost equivalent performances on D2SA are achieved, while reducing the number of costly human-labeled real images for finetuning. Figure 23 shows that a bicameral network finetuned on D2SA, with the first three encoder blocks frozen after pretraining on Mikado, using only 25% of the initial D2SA finetuning subset still outperforms a bicameral network trained only on D2SA or D2SA+.

Synthetic data for learning better transferable invariants
Unlike real-world datasets, a synthetic dataset is readily extensible. By enriching Mikado with 20 times more

texture images, 15 times more background images and 4 mesh templates, namely Mikado+, we expect more transferable local and global invariants to be learned as the ranges of color, texture, shape, and pose variations are better represented. Table 9 indeed reports that pretraining on Mikado+ instead of training only on D2SA increases AP by 10.1 points for boundaries and 7.8 points for occlusions while using only 13% of the initial D2SA finetuning set (Figure 23). This corresponds to a gain of 3.4 points for boundaries and 4.1 points for occlusions over using Mikado in the same conditions. These observations imply that Mikado+ enables to learn more abstract local representations than Mikado. However, when applied on D2SA without finetuning, the Mikado+ model proves less effective than the model pretrained on Mikado. Consistently with the results after finetuning on D2SA, this could be explained by an overgeneralization of the task-specific layers. The neurons indeed co-adapt to capture the most discriminative patterns that are not likely to be the colors nor the object and background textures in Mikado+. An over-randomization of the colors and textures may disconnect the learned representations from concrete examples. This has nevertheless the advantage of easing the finetuning on D2SA, as the real-world scenes then appear as a specific variation consistent with the learned abstract representations. All these observations are incentives to favour synthetic training data when pixel-wise annotations on real-world images are hardly collectable. Hand-made annotations may also hinder the training due to their inaccuracy and incompleteness. As illustrated by Figure 24, the bicameral network is able to fairly predict non-annotated boundaries, *e.g.* internal boundaries of instances with holes, missing instances, or instances ambiguously considered as part of the back-

ground. Furthermore, objects with complex shape, such as houseplants, which are often coarsely annotated by humans, are finely delineated by the proposed network.

7 Conclusion

In this paper, we addressed the problem of delineating object instances and inferring their spatial layout from a single RGB image. Unlike the state-of-the-art approach which consists in two independent FCN streams, we argued that boundaries and occlusions can be obtained from a joint feature space. As a result, we proposed a parameter-saving network design composed of a single encoder shared by two cascaded decoders through skip-layer connections, for jointly predicting instance boundaries and their unoccluded side. Furthermore, as occlusions between instances are under-represented in the related state-of-the-art datasets (PIOD, COCOA, D2SA), which are costly to extend as they contain manually annotated real images, we introduced a pipeline for generating synthetic images of textured objects piled up in bulk, namely Mikado. Our ablation study and comparative experiments with the two-stream baseline and alternative architectures showed that the proposed bicameral structuring gives the best overall results on both PIOD and Mikado. The proposed design, which postpones instance localization, also outperforms on COCOA the state-of-the-art amodal segmentation approach, which by contrast rely on rectangle region proposals to first isolate instances. We finally proved that our synthetic imagery is plausible for real-world applications. Our experiments on transfer learning from Mikado to D2SA showed that using local synthetic features enables better real-world performances than using only real images. We also highlighted that enriching the synthetic data distribution enables to extract more abstract representations, thus achieving state-of-the-art performances while reducing by more than 85% the number of real images for finetuning. As future work, we plan to further our results on joint representation learning for multiple tasks by exploring a “multicameral” FCN-based structuring for jointly inferring the instance locations and categories as well. We also consider more advanced unsupervised domain adaptation techniques to bridge the reality gap without the need of annotated real images, while building a significantly larger synthetic dataset for real-world robotic setups.

References

1. R. Deng, C. Shen, S. Liu, H. Wang, X. Liu, Learning to Predict Crisp Boundaries, in *ECCV (6)*, *Lecture Notes in Computer Science*, vol. 11210, ed. by V. Ferrari, M. Hebert, C. Sminchisescu, Y. Weiss (Springer, 2018), *Lecture Notes in Computer Science*, vol. 11210, pp. 570–586
2. Y. Wang, X. Zhao, K. Huang, Deep Crisp Boundaries, in *CVPR* (IEEE Computer Society, 2017), pp. 1724–1732
3. Y. Liu, M.M. Cheng, X. Hu, K. Wang, X. Bai, Richer Convolutional Features for Edge Detection, in *CVPR* (IEEE Computer Society, 2017), pp. 5872–5881
4. J. Yang, B.L. Price, S. Cohen, H. Lee, M.H. Yang, Object Contour Detection with a Fully Convolutional Encoder-Decoder Network, in *CVPR* (IEEE Computer Society, 2016), pp. 193–202
5. O. Ronneberger, P. Fischer, T. Brox, *U-Net: Convolutional Networks for Biomedical Image Segmentation* (Springer International Publishing, 2015), pp. 234–241. DOI 10.1007/978-3-319-24574-4_28. URL https://doi.org/10.1007/978-3-319-24574-4_28
6. S. Xie, Z. Tu, Holistically-Nested Edge Detection, in *ICCV* (IEEE Computer Society, 2015), pp. 1395–1403
7. L.C. Chen, Y. Zhu, G. Papandreou, F. Schroff, H. Adam, Encoder-Decoder with Atrous Separable Convolution for Semantic Image Segmentation, in *ECCV (7)*, *Lecture Notes in Computer Science*, vol. 11211, ed. by V. Ferrari, M. Hebert, C. Sminchisescu, Y. Weiss (Springer, 2018), *Lecture Notes in Computer Science*, vol. 11211, pp. 833–851
8. V. Badrinarayanan, A. Kendall, R. Cipolla, SegNet: A Deep Convolutional Encoder-Decoder Architecture for Image Segmentation, *IEEE Transactions on Pattern Analysis and Machine Intelligence (TPAMI)* **39**(12), 2481 (2017)
9. A. Nguyen, D. Kanoulas, D.G. Caldwell, N.G. Tsagarakis, Detecting object affordances with Convolutional Neural Networks, in *IROS* (IEEE, 2016), pp. 2765–2770
10. J. Long, E. Shelhamer, T. Darrell, Fully Convolutional Networks for Semantic Segmentation, in *CVPR* (2015)
11. J. Pont-Tuset, P. Arbelaez, J.T. Barron, F. Marqus, J. Malik, Multiscale Combinatorial Grouping for Image Segmentation and Object Proposal Generation, *IEEE Transactions on Pattern Analysis and Machine Intelligence* **39**(1), 128 (2017)
12. C. Wang, L. Zhao, S. Liang, L. Zhang, J. Jia, Y. Wei, Object proposal by multi-branch hierarchical segmentation, in *CVPR* (IEEE Computer Society, 2015), pp. 3873–3881
13. M. Bai, R. Urtasun, Deep Watershed Transform for Instance Segmentation, in *CVPR* (IEEE Computer Society, 2017), pp. 2858–2866
14. G. Li, Y. Xie, L. Lin, Y. Yu, Instance-Level Salient Object Segmentation, in *CVPR* (IEEE Computer Society, 2017), pp. 247–256
15. A. Arnab, P.H.S. Torr, Pixelwise Instance Segmentation with a Dynamically Instantiated Network, in *CVPR* (IEEE Computer Society, 2017), pp. 879–888
16. S. Liu, L. Qi, H. Qin, J. Shi, J. Jia, Path Aggregation Network for Instance Segmentation, in *CVPR* (IEEE Computer Society, 2018), pp. 8759–8768
17. R. Hu, P. Dollr, K. He, T. Darrell, R.B. Girshick, Learning to Segment Every Thing, in *CVPR* (IEEE Computer Society, 2018)
18. T.T. Do, A. Nguyen, I.D. Reid, AffordanceNet: An End-to-End Deep Learning Approach for Object Affordance Detection, in *ICRA* (IEEE, 2018), pp. 1–5
19. K. He, G. Gkioxari, P. Dollár, R.B. Girshick, Mask R-CNN, in *ICCV* (IEEE Computer Society, 2017), pp. 2980–2988
20. J. Redmon, A. Farhadi, YOLO9000: Better, Faster, Stronger, in *CVPR* (IEEE Computer Society, 2017), pp. 6517–6525

21. S. Ren, K. He, R.B. Girshick, J. Sun, Faster R-CNN: Towards Real-Time Object Detection with Region Proposal Networks, in *NIPS* (2015), pp. 91–99
22. X. Ren, C.C. Fowlkes, J. Malik, Figure/Ground Assignment in Natural Images, in *ECCV*, vol. 3952, ed. by A. Leonardis, H. Bischof, A. Pinz (Berlin, Heidelberg, 2006), vol. 3952, pp. 614–627
23. P. Wang, A.L. Yuille, DOC: Deep OCclusion Estimation from a Single Image, in *ECCV (1)*, *Lecture Notes in Computer Science*, vol. 9905, ed. by B. Leibe, J. Matas, N. Sebe, M. Welling (Springer, 2016), *Lecture Notes in Computer Science*, vol. 9905, pp. 545–561
24. Y. Zhu, Y. Tian, D.N. Metaxas, P. Dollár, Semantic Amodal Segmentation, in *CVPR* (IEEE Computer Society, 2017), pp. 3001–3009
25. P. Follmann, T. Böttger, P. Härtinger, R. König, M. Ulrich, MVTEc D2S: Densely Segmented Supermarket Dataset, in *ECCV (10)*, *Lecture Notes in Computer Science*, vol. 11214, ed. by V. Ferrari, M. Hebert, C. Sminchisescu, Y. Weiss (Springer, 2018), *Lecture Notes in Computer Science*, vol. 11214, pp. 581–597
26. C. Feichtenhofer, A. Pinz, A. Zisserman, Convolutional Two-Stream Network Fusion for Video Action Recognition, in *CVPR* (IEEE Computer Society, 2016), pp. 1933–1941
27. K. Simonyan, A. Zisserman, Two-Stream Convolutional Networks for Action Recognition in Videos, in *NIPS*, ed. by Z. Ghahramani, M. Welling, C. Cortes, N.D. Lawrence, K.Q. Weinberger (2014), pp. 568–576
28. Y. Zhu, Y. Tian, D.N. Metaxas, P. Dollár, Semantic Amodal Segmentation, in *CVPR* (IEEE Computer Society, 2017), pp. 3001–3009
29. C.L. Teo, C. Fermller, Y. Aloimonos, Fast 2D border ownership assignment, in *CVPR* (IEEE Computer Society, 2015), pp. 5117–5125
30. M. Maire, Simultaneous Segmentation and Figure/Ground Organization Using Angular Embedding, in *European Conf. on Computer Vision (2)* (2010), pp. 450–464
31. H. Fu, C. Wang, D. Tao, M.J. Black, Occlusion Boundary Detection via Deep Exploration of Context, in *CVPR* (IEEE Computer Society, 2016), pp. 241–250
32. K. He, X. Zhang, S. Ren, J. Sun, Deep Residual Learning for Image Recognition, in *CVPR* (IEEE Computer Society, 2016), pp. 770–778
33. K. Simonyan, A. Zisserman, Very Deep Convolutional Networks for Large-Scale Image Recognition, in *International Conference on Learning Representations (ICLR)* (IEEE Computer Society, 2015)
34. C.L. Zitnick, T. Kanade, A Cooperative Algorithm for Stereo Matching and Occlusion Detection, *IEEE Transactions on Pattern Analysis Machine Intelligence (TPAMI)* **22**(7), 675 (2000)
35. N. Grammalidis, M.G. Strintzis, Disparity and occlusion estimation in multiocular systems and their coding for the communication of multiview image sequences, *IEEE Trans. Circuits Syst. Video Techn.* **8**(3), 328 (1998)
36. D. Geiger, B. Ladendorf, A.L. Yuille, Occlusions and binocular stereo, *International Journal of Computer Vision* **14**(3), 211 (1995)
37. D. Sun, C. Liu, H. Pfister, Local Layering for Joint Motion Estimation and Occlusion Detection, in *CVPR* (IEEE Computer Society, 2014), pp. 1098–1105
38. A. Ayvaci, M. Raptis, S. Soatto, Sparse Occlusion Detection with Optical Flow, *International Journal of Computer Vision* **97**(3), 322 (2012)
39. A. Humayun, O. Mac Aodha, G.J. Brostow, Learning to find occlusion regions, in *CVPR* (IEEE Computer Society, 2011), pp. 2161–2168
40. X. He, A. Yuille, in *European Conference on Computer Vision (ECCV)*, vol. 6314 (2010), pp. 539–552
41. A. Ayvaci, M. Raptis, S. Soatto, Occlusion Detection and Motion Estimation with Convex Optimization, in *NIPS*, ed. by J.D. Lafferty, C.K.I. Williams, J. Shawe-Taylor, R.S. Zemel, A. Culotta (Curran Associates, Inc., 2010), pp. 100–108
42. A. Stein, M. Hebert, Local Detection of Occlusion Boundaries in Video, in *British Machine Vision Conf.* (2006)
43. O. Williams, M. Isard, J. MacCormick, Estimating Disparity and Occlusions in Stereo Video Sequences, in *CVPR (2)* (IEEE Computer Society, 2005), pp. 250–257
44. F. Liu, C. Shen, G. Lin, I.D. Reid, Learning Depth from Single Monocular Images Using Deep Convolutional Neural Fields, *IEEE Transactions on Pattern Analysis Machine Intelligence* **38**(10), 2024 (2016)
45. B. Li, C. Shen, Y. Dai, A. van den Hengel, M. He, Depth and surface normal estimation from monocular images using regression on deep features and hierarchical CRFs, in *CVPR* (IEEE Computer Society, 2015), pp. 1119–1127
46. D. Eigen, C. Puhrsch, R. Fergus, Depth Map Prediction from a Single Image using a Multi-Scale Deep Network, in *NIPS* (2014), pp. 2366–2374
47. D.R. Martin, C.C. Fowlkes, J. Malik, Learning to Detect Natural Image Boundaries Using Local Brightness, Color, and Texture Cues, *TPAMI* **26**(5), 530 (2004). DOI 10.1109/TPAMI.2004.1273918
48. D. Hoiem, A.N. Stein, A.A. Efros, M. Hebert, Recovering Occlusion Boundaries from a Single Image, in *ICCV* (IEEE Computer Society, 2007), pp. 1–8
49. P. Dollár, C.L. Zitnick, Structured Forests for Fast Edge Detection, in *ICCV* (IEEE Computer Society, 2013), pp. 1841–1848
50. M. Maire, T. Narihira, S.X. Yu, Affinity CNN: Learning Pixel-Centric Pairwise Relations for Figure/Ground Embedding, in *CVPR* (IEEE Computer Society, 2016), pp. 174–182
51. P. Luo, G. Wang, L. Lin, X. Wang, Deep Dual Learning for Semantic Image Segmentation, in *ICCV* (IEEE Computer Society, 2017), pp. 2737–2745
52. A. Odena, V. Dumoulin, C. Olah, Deconvolution and Checkerboard Artifacts, *Distill* (2016). DOI 10.23915/distill.00003. URL <http://distill.pub/2016/deconv-checkerboard>
53. Huang, Gao and Liu, Zhuang and van der Maaten, Laurens and Weinberger, Kilian Q., Densely Connected Convolutional Networks, in *CVPR* (IEEE Computer Society, 2017), pp. 2261–2269
54. Z. Yu, W. Liu, Y. Zou, C. Feng, S. Ramalingam, B.V.K.V. Kumar, J. Kautz, Simultaneous Edge Alignment and Learning, in *ECCV (3)*, *Lecture Notes in Computer Science*, vol. 11207, ed. by V. Ferrari, M. Hebert, C. Sminchisescu, Y. Weiss (Springer, 2018), *Lecture Notes in Computer Science*, vol. 11207, pp. 400–417
55. T.Y. Lin, P. Goyal, R.B. Girshick, K. He, P. Dollr, Focal Loss for Dense Object Detection, in *ICCV* (IEEE Computer Society, 2017), pp. 2999–3007
56. D. Martin, C. Fowlkes, D. Tal, J. Malik, A Database of Human Segmented Natural Images and its Application to Evaluating Segmentation Algorithms and Measuring Ecological Statistics, in *Proc. 8th Int'l Conf. Computer Vision*, vol. 2 (2001), vol. 2, pp. 416–423
57. M. Everingham, L. Van Gool, C.K.I. Williams, J. Winn, A. Zisserman, The PASCAL Visual Object Classes

Challenge 2012 (VOC2012) Results. <http://www.pascal-network.org/challenges/VOC/voc2012/workshop/index.html>

58. T.Y. Lin, M. Maire, S. Belongie, J. Hays, P. Perona, D. Ramanan, P. Dollár, C.L. Zitnick, Microsoft COCO: Common Objects in Context, in *ECCV (5)*, *Lecture Notes in Computer Science*, vol. 8693, ed. by D.J. Fleet, T. Pajdla, B. Schiele, T. Tuytelaars (Springer, 2014), *Lecture Notes in Computer Science*, vol. 8693, pp. 740–755
59. M. Grard, R. Brégier, F. Sella, E. Dellandréa, L. Chen, in *2017 International Workshop on Human-Friendly Robotics, Springer Proceedings in Advanced Robotics*, vol. 7 (Springer, 2018). URL <https://arxiv.org/abs/1801.01281>
60. R. Brégier, F. Devernay, L. Leyrit, J.L. Crowley, Symmetry Aware Evaluation of 3D Object Detection and Pose Estimation in Scenes of Many Parts in Bulk, in *ICCV Workshops* (IEEE Computer Society, 2017), pp. 2209–2218
61. Blender Online Community, *Blender - a 3D modelling and rendering package*. Blender Foundation, Blender Institute, Amsterdam (2016). URL <http://www.blender.org>
62. J. Yosinski, J. Clune, Y. Bengio, H. Lipson, How transferable are features in deep neural networks?, in *Annual Conference on Neural Information Processing Systems (NIPS)*, ed. by Z. Ghahramani, M. Welling, C. Cortes, N.D. Lawrence, K.Q. Weinberger (2014), pp. 3320–3328
63. S. Ben-David, T. Lu, T. Luu, D. Pl, Impossibility Theorems for Domain Adaptation, in *AISTATS, JMLR Proceedings*, vol. 9, ed. by Y.W. Teh, D.M. Titterington (JMLR.org, 2010), *JMLR Proceedings*, vol. 9, pp. 129–136
64. S. Ben-David, J. Blitzer, K. Crammer, A. Kulesza, F. Pereira, J.W. Vaughan, A theory of learning from different domains., *Machine Learning* **79**(1-2), 151 (2010)
65. H. Caesar, J.R.R. Uijlings, V. Ferrari, COCO-Stuff: Thing and Stuff Classes in Context, in *CVPR* (IEEE Computer Society, 2018), pp. 1209–1218
66. Y. Jia, E. Shelhamer, J. Donahue, S. Karayev, J. Long, R. Girshick, S. Guadarrama, T. Darrell, Caffe: Convolutional Architecture for Fast Feature Embedding, arXiv preprint arXiv:1408.5093 (2014)
67. D.P. Kingma, J. Ba, Adam: A Method for Stochastic Optimization, in *Proceedings of the International Conference on Learning Representations (ICLR)* (2015)
68. O. Russakovsky, J. Deng, H. Su, J. Krause, S. Satheesh, S. Ma, Z. Huang, A. Karpathy, A. Khosla, M. Bernstein, A.C. Berg, L. Fei-Fei, ImageNet Large Scale Visual Recognition Challenge, *International Journal of Computer Vision (IJCV)* **115**(3), 211 (2015). DOI 10.1007/s11263-015-0816-y
69. X. Glorot, Y. Bengio, Understanding the difficulty of training deep feedforward neural networks, in *International Conference on Artificial Intelligence and Statistics (AISTATS), JMLR Proceedings*, vol. 9, ed. by Y.W. Teh, D.M. Titterington (JMLR.org, 2010), *JMLR Proceedings*, vol. 9, pp. 249–256
70. K.K. Maninis, J. Pont-Tuset, P.A. Arbelaez, L.J.V. Gool, Convolutional Oriented Boundaries, in *ECCV (1)*, *Lecture Notes in Computer Science*, vol. 9905, ed. by B. Leibe, J. Matas, N. Sebe, M. Welling (Springer, 2016), *Lecture Notes in Computer Science*, vol. 9905, pp. 580–596
71. G. Bertasius, J. Shi, L. Torresani, High-for-Low and Low-for-High: Efficient Boundary Detection from Deep Object Features and Its Applications to High-Level Vision, in *ICCV* (IEEE Computer Society, 2015), pp. 504–512
72. W. Shen, X. Wang, Y. Wang, X. Bai, Z. Zhang, DeepContour: A deep convolutional feature learned by positive-sharing loss for contour detection, in *CVPR* (IEEE Computer Society, 2015), pp. 3982–3991
73. G. Bertasius, J. Shi, L. Torresani, DeepEdge: A multi-scale bifurcated deep network for top-down contour detection, in *CVPR* (IEEE Computer Society, 2015), pp. 4380–4389
74. S. Gupta, R.B. Girshick, P.A. Arbelaez, J. Malik, Learning Rich Features from RGB-D Images for Object Detection and Segmentation, in *ECCV (7)*, *Lecture Notes in Computer Science*, vol. 8695, ed. by D.J. Fleet, T. Pajdla, B. Schiele, T. Tuytelaars (Springer, 2014), *Lecture Notes in Computer Science*, vol. 8695, pp. 345–360
75. J.J. Lim, C.L. Zitnick, P. Dollár, Sketch Tokens: A Learned Mid-level Representation for Contour and Object Detection, in *CVPR* (IEEE Computer Society, 2013), pp. 3158–3165
76. P. Arbelaez, M. Maire, C. Fowlkes, J. Malik, Contour detection and hierarchical image segmentation, *IEEE TPAMI* **33**(5), 898 (2011). DOI 10.1109/TPAMI.2010.161